Speciation and fate of trace metals in estuarine sediments under reduced and oxidized conditions, Seaplane Lagoon, Alameda Naval Air Station (USA)

Susan Carroll,[a] Peggy A. O'Day,[b] Brad Esser[a] and Simon Randall[c]

[a]*Lawrence Livermore National Laboratory, Livermore, CA 94550, USA*
[b]*Department of Geological Sciences, Arizona State University, Tempe, AZ 85287, USA*
[c]*Department of Earth Sciences, University of Bristol, Bristol, England BS8 1RJ*

Paper

Received 27th May 2002, Accepted 16th October 2002
First published as an Advance Article on the web 20th November 2002

We have identified important chemical reactions that control the fate of metal-contaminated estuarine sediments if they are left undisturbed (*in situ*) or if they are dredged. We combined information on the molecular bonding of metals in solids from X-ray absorption spectroscopy (XAS) with thermodynamic and kinetic driving forces obtained from dissolved metal concentrations to deduce the dominant reactions under reduced and oxidized conditions. We evaluated the *in situ* geochemistry of metals (cadmium, chromium, iron, lead, manganese and zinc) as a function of sediment depth (to 100 cm) from a 60 year record of contamination at the Alameda Naval Air Station, California. Results from XAS and thermodynamic modeling of porewaters show that cadmium and most of the zinc form stable sulfide phases, and that lead and chromium are associated with stable carbonate, phosphate, phyllosilicate, or oxide minerals. Therefore, there is minimal risk associated with the release of these trace metals from the deeper sediments contaminated prior to the Clean Water Act (1975) as long as reducing conditions are maintained. Increased concentrations of dissolved metals with depth were indicative of the formation of metal HS^- complexes. The sediments also contain zinc, chromium, and manganese associated with detrital iron-rich phyllosilicates and/or oxides. These phases are recalcitrant at near-neutral pH and do not undergo reductive dissolution within the 60 year depositional history of sediments at this site.

The fate of these metals during dredging was evaluated by comparing *in situ* geochemistry with that of sediments oxidized by seawater in laboratory experiments. Cadmium and zinc pose the greatest hazard from dredging because their sulfides were highly reactive in seawater. However, their dissolved concentrations under oxic conditions were limited eventually by sorption to or co-precipitation with an iron (oxy)hydroxide. About 50% of the reacted CdS and 80% of the reacted ZnS were bonded to an oxide-substrate at the end of the 90-day oxidation experiment. Lead and chromium pose a minimal hazard from dredging because they are bonded to relatively insoluble carbonate, phosphate, phyllosilicate, or oxide minerals that are stable in seawater. These results point out the specific chemical behavior of individual metals in estuarine sediments, and the need for direct confirmation of metal speciation in order to constrain predictive models that realistically assess the fate of metals in urban harbors and coastal sediments.

1. Introduction

A recent evaluation of sediment contamination of surface waters in the United States by the US Environmental Protection Agency identified 96 watersheds, mostly urban harbors, containing metal and/or organic chemical contents that are potentially hazardous to aquatic biota.[1] These harbors and coastal sediments are contaminated from past and present industrial and military waste disposal practices. One such example is the estuary sediments of the East Outfall Site of the Seaplane Lagoon, at the former Naval Air Station (NAS) Alameda located on an island in San Francisco Bay, USA (Fig. 1). The most abundant metals in the sediments are cadmium, lead, chromium, zinc, copper, and nickel. Concentrations of these metal contaminants above background levels in San Francisco Bay result from a 57 year history of military and industrial activity at this site. From 1940 to 1975, the Seaplane Lagoon received about 300 million gallons of wastewater from industrial and storm sewers from NAS Alameda. The Seaplane Lagoon and its surrounding area have been designated as a mixed-use commercial marina site in the City of Alameda land use plan.[2] A concern for this site and other urban estuarine environments is the contamination of the overlying water column as metals dissolve when reduced sediments react with oxygen-rich water during bioturbation, storm, dredging and other marina activities.

Recent studies of metal contamination in the San Francisco Bay identified previously contaminated sediments as a major source for some metals in the water column. Rivera-Duarte and Flegal calculated the total benthic fluxes of lead,[3] silver,[4] cadmium, cobalt, copper, nickel, and zinc[5] using measured porewater concentrations and a flux equation that combines Fickian diffusion and an irrigation flux from bioturbation and mixing of the top sediments. They found that the relative benthic to fluvial inputs to the San Francisco Bay were metal specific. Lead inputs from the sediments were 30 to 930 times fluvial inputs. Silver release from the sediments near wastewater treatment outflows contributed about 2.5 times the input of the fluvial system for the entire San Francisco Bay. Benthic and fluvial inputs were similar for zinc, but nickel, cadmium, and copper showed small or negative fluxes from the sediments to the overlying waters. This approach is a useful metric to

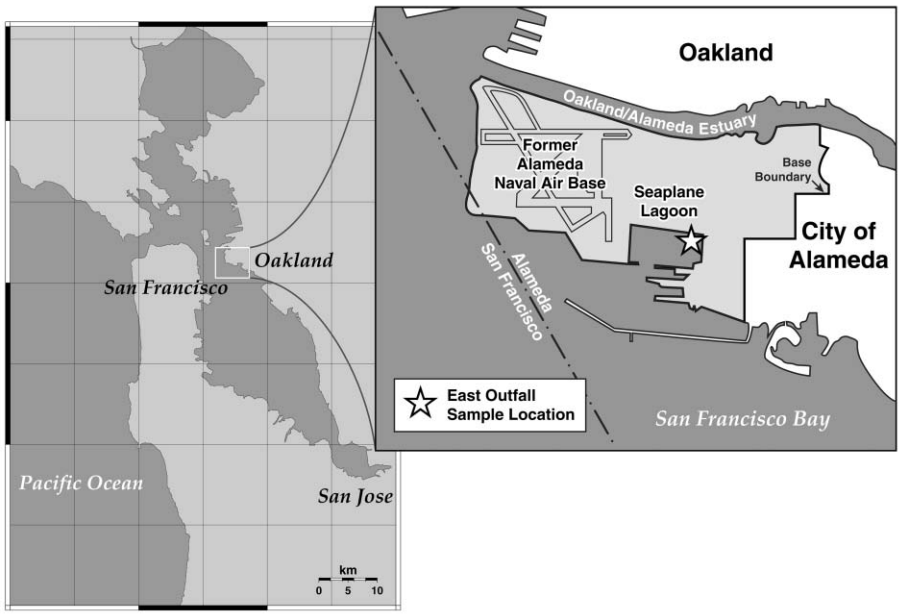

Fig. 1 Location map of field study. Star indicates general location where the sediment cores were sampled.

compare metal contamination sources in large watersheds, but it does not explicitly account for the geochemical reactions that control the porewater concentrations.

Important chemical controls on the flux of trace metals to the water column are the oxidation and reduction of sulfur and iron in surfacial estuarine sediments, as indicated by *in situ* measurement of trace metal fluxes across the sediment – water boundary in Gullmarsfjorden.[6,7] In these studies, high fluxes of cadmium, copper, and zinc from the sediments to the overlying water in the oxygen-enhanced portion of the experiment were reversed when the overlying water went anoxic and trace metals were transferred to the sediments. However, the iron flux showed the opposite trend with a negative flux to the sediments during oxidation and positive flux to the water column as they became anoxic. The negative correlation between these trace metals and iron and the reported lack of correlation with carbonate flux suggests that cadmium, copper, and zinc are present in the sediments as sulfides which can be easily dissolved by oxygen-rich waters. The increase in dissolved iron as the sediments become anoxic represents the reductive dissolution of iron hydroxides that formed during the oxidation experiment. *In situ* measurements of this kind provide valuable insight into trace metal geochemistry, but final interpretation of the data lack confirmation of the reactions in the solid phases in the sediment.

Much of our knowledge of the solid chemical form of trace metals in reduced estuarine sediments has been derived indirectly from water analyses and from chemical extractions. Although there is ambiguity among studies, trace metal uptake in the sediments is often linked to iron sulfides such as pyrite (FeS_2) and monosulfides (amorphous FeS or mackinawite). For example, Kornicker and Morse[8] reported cadmium, manganese, and nickel sorption to pyrite in solution-based experiments. In estuarine sediments, copper and manganese have been identified as pyrite co-precipitates because they dissolved in the pyrite extraction. In contrast, cadmium, chromium, lead, and zinc are believed to be sequestered by other sulfides or oxides because a significant amount of these metals dissolved with less aggressive, non-pyrite extractions.[9] Similarly trace metal sorption or co-precipitation with amorphous FeS or mackinawite have been observed.[10,11] An improved method to the use of chemical extractions is to determine trace metal bonding in sediments using synchrotron radiation X-ray absorption spectroscopy (XAS). This method is a unique molecular probe for complex materials because it is element specific, has relatively high sensitivity, does not require a vacuum, and is non-destructive. Thus, spectra for a number of elements can be directly measured on a bulk, untreated sediment samples with porewater present.

In this paper, we have examined the chemical processes that impact the fate of metal contaminated estuarine sediments if they are left undisturbed (*in situ*) or if they are dredged. We discuss the *in situ* geochemistry of metals (cadmium, chromium, copper, lead, manganese nickel, and zinc) with variation of depth in contaminated estuarine sediments from one site in the Seaplane Lagoon. We also discuss the geochemical processes responsible for the transfer of these metals from reduced contaminated estuarine sediments to oxygen-rich seawater by comparing *in situ* geochemistry with that of the oxidized sediments. To do this, we combine bulk sediment and porewater analyses, flow-through oxidation experiments, geochemical modeling, and X-ray absorption spectroscopy. Combination of the geochemical and spectroscopic data yields a more robust picture of the reactions that control the fate of trace metal contaminates in urban harbors and coastal sediments.

2. Methods

2.1. Sample collection and analysis

Between July 1997 and November 1998, a series of sediment cores were collected from the East Outfall Site, Seaplane Lagoon (Fig. 1). For the geochemical and spectroscopic results given here, we focus on 0.5 m Plexiglas push cores that were collected on July 10, 1997 and on November 10, 1997 within the same general location (GH-CC-SC2, GH-CC-SC4, GH-CC-SC7, and GH-CC-SC9; referred to here as SC2, SC4, SC7, and SC9). Sediment cores were sectioned under argon and subsamples taken at 3 cm intervals from the center portion of the core to ensure no oxidation. Sediment compositions are reported for the push cores SC2 to SC4 and for deeper gravity cores to 1 m (GH-CC-C1, GH-CC-C2 and GH-CC-C3; referred to here as C1, C2, and C3). From core SC4, we extracted porewater for sulfur, chloride, trace and major element concentrations by centrifugation (5000 rpm for 60 min in argon-filled centrifuge tubes) and filtration (using 0.22 μm polycarbonate filters), and we measured wet sediment pH. From core SC2, we extracted porewater by Reeburgh-type

pneumatic core squeezers in a nitrogen glove box for total phosphorus, sulfur and carbon concentrations. Synchrotron X-ray absorption spectroscopy (XAS) data were collected from frozen samples stored in N_2 (SC2, SC4, C1, C3) and from fresh, unfrozen sediments (SC7, SC9) within days of core recovery maintaining the oxic water column. Based on comparisons of fresh and frozen samples, freezing and thawing the sediments under controlled environments did not alter the metal chemistry.

2.2. Sediment oxidation experiments

Three samples of reduced Seaplane Lagoon sediment from core SC4 at 31.5 cm (SC4-11) were reacted with filtered, oxygen-rich seawater for 92 days to determine the net metal dissolution and changes in sediment metal coordination. The seawater (pH = 7.9) was collected offshore from the Pacific Ocean by Long's Marine Laboratory, University of California, Santa Cruz. The experiments were performed in well-mixed, flow-through reactors at room temperature.[12] Reaction vessels and sample bottles were cleaned in a Class 100 clean room. Twenty samples were collected during the experiment and sample pH was measured immediately after the sample was collected. Samples for trace element analysis were acidified with ultra-pure nitric acid to prevent precipitation. Sample bottles were double bagged and stored in a laminar flow hood until they were analyzed in a Class 100 clean room. An identical control experiment with seawater and no sediment was also run to provide procedural blanks.

2.3. Water analyses

2.3.1. Trace metals. Seaplane Lagoon porewaters and output solutions from the oxidation experiments were analyzed for Al, Cd, Cr, Cu, Fe, Pb, Mn, Ni, and Zn using a Hewlett-Packard HP4500 inductively coupled plasma-mass spectrometer (ICP-MS). An isotope dilution method was used to measure the porewater Cd, Cr, Cu, Pb, Ni, and Zn concentrations, by equilibrating the samples with a mixed enriched isotope spike (^{111}Cd, ^{52}Cr, ^{65}Cu, ^{206}Pb, ^{61}Ni, ^{67}Zn) at temperature for 48 h, and then concentrating the trace metals from the equilibrated porewater by precipitating $Mg(OH)_2$ from seawater at pH 10, which scavenges a number of trace metals. The precipitate was then carefully washed with pH 10 ultra-pure ammonium hydroxide solution to remove sea salts, and then dissolved in 2% ultra-pure nitric acid for trace metal analyses[13] Because Cd and Ni were not concentrated on the $Mg(OH)_2$ precipitate, the supernatant and washes were combined and concentrated using a Cetac Corporation DSX-100 system. Cd and Ni were run under normal plasma conditions, Cr and Cu were run under cool plasma conditions to reduce interference from ArC and ArMg, and Pb and Zn were run under hot plasma conditions to enhance sensitivity at high masses. For all isotope dilution determinations, the error in the measured ratios was less than 10% and generally in the range of 1–4%, and precision was 10–15% for Cr, Ni, Cd and Pb; and 15–20% for Cu and Zn.

For the porewater Al, Mn, and Fe analyses, aliquots of the saline porewater were diluted to 1 psu (practical salinity unit) with ultra-pure 2% nitric acid and spiked with Sc and Y as internal standards and run under normal plasma conditions. Calibration curves were made in a seawater reference standard (NASS-4) diluted to 1 psu to correct for matrix effects. Detection limits determined from the reproducibility of procedural blanks were 1 ng g^{-1} for Al, 0.1 ng g^{-1} for Mn, and 100 ng g^{-1} for Fe, and precision was generally less than 5–10%.

Filtered output samples from the oxidation experiments were concentrated 5 to 10 times using a Cetac Corporation DSX-100 system, spiked with Sc, Y, In, Tb, and Bi internal standards to correct for matrix effects and instrument drift, and run under hot plasma conditions. Calibration curves were made in a series of standards in 2% ultra-pure nitric acid. Reported errors include both measurement and calibration uncertainties. Detection limits were determined by processing ion-exchange resin beads through the DSX-100 chemistry under the same conditions as the output samples. No significant differences were seen in different batches of resin. Accuracy was measured against metal concentrations in two seawater reference standards, NASS-4 and CASS-3.

2.3.3. Major elements, sulfur, chloride, and carbon analyses. Total dissolved Al, Ca, Fe, K, Mg, Mn, Na, P, S, and Si were analyzed by a Fisons Instruments (Model 3560) inductively coupled plasma-atomic emission spectrometer against multi-point calibration curves in distilled and deionized water. The reproducibility of this technique was better than 2%. Sulfur speciation and concentrations were determined by ion chromatography (Beckman 421A controller, a LDC Milton Roy Conducto Monitor III conductivity detector, and a Waters 4.6 × 150 mm IC-Pak Anion HC column) against multi-point calibration curves. Samples were injected in a helium-purged, 5 mM sodium phosphate solution. Detection limit was 5 mg L^{-1} for each sulfur species, and precision and accuracy were better than 10%. Chloride concentrations were determined using an ion-specific probe against a multi-point NaCl calibration curve in distilled and deionized water. The detection limit was 10 ng g^{-1}, and precision and accuracy were better than 10%. Dissolved carbon analyses were made with an infrared carbon analyzer (O. I. Analytical TOC 700). Total inorganic carbon (TIC) and total organic carbon (TOC) were measured in sequence by first acidifying the sample to pH < 4, heating it to 100 °C, and trapping and detecting the evolved CO_2. The dissolved organic carbon in the sample was then oxidized with sodium persulfate at 100 °C and the evolved CO_2 was trapped and detected. Total carbon (TC) was measured directly by combining the TIC and TOC methods into a single step.

2.4. Bulk sediment chemistry and mineralogy

2.4.1. Sediment digestion. The chemical depth profiles were determined for cores SC2-4 and C1-3 from sediment samples digested with acid UA2 solutions (mixture of concentrated HF and HCl from Unisolv, Inc.) in a microwave and neutralized and stabilized with UNS2A/2B solutions (mixtures of H_3BO_3, TETA and EDTA from Unisolv, Inc.). Reported Al, Ca, Cd, Co, Cr, Cu, Fe, Mg, Mn, Ni, Pb, S, and Zn concentrations were analyzed by inductively coupled plasma-atomic emission spectrometry. Analysis protocol adheres to EPA SW-846 Method 6010A augmented to include all of the elements listed above. A scandium spike was added to all samples to correct for viscosity effects resulting from the high silica content of these sediments and instrument drift. Detection limits and analytical reproducibility are reported in the data. The quartz content prevented recovery of silica concentrations because silica did not stay in solution. The external standard was the NIST Buffalo River sediment.

2.4.2. X-ray diffraction. Sediment mineralogy was determined by X-ray diffraction (XRD) on freeze dried and ground sediment samples from cores SC2-4 and C1-3. Data were collected from random orientation powder samples with a Scintag PAD V instrument using a Cu-Kα source at 45 kV and 35 mA from 2 to 92° 2θ in 0.02° steps. XRD cannot detect amorphous solids or minerals that are present at <2 wt%. For a few samples, XRD spectra were collected on air-dried and ethylene glycol-saturated sediments to separate some of the diagnostic clay peaks (*e.g.*, smectite from chlorite). Reported mineral abundance is estimated by assigning minimum XRD detection limits to the trace mineral components (~2 wt%).

2.5. XAS data collection and analysis

X-ray absorption spectroscopy (XAS), including X-ray absorption near-edge structure (XANES) and extended X-ray absorption fine structure (EXAFS) analyses, were used to characterize the speciation and bonding of metals in sediments from cores. Fluorescence spectra were collected at Stanford Synchrotron Radiation Laboratory (SSRL) on wiggler beamlines 4-1 and 4-3 using either a 13-element Ge array detector, a 4-element Ge array detector, or a Lytle detector. Either a Si(111) or Si(220) monochromator crystal was used, depending on which crystal produced the higher quality spectra for a given element, and detuned 50–70% of maximum intensity to minimize higher-order harmonic reflections. XANES spectra for chrominum and manganese were collected with a Si(220) crystal to achieve higher energy resolution. Spectra were collected at ambient temperature with the sample in an helium atmosphere to prevent oxidation of sensitive elements. For a given element, energy was calibrated using a reference foil spectrum. Absorption spectra for crystalline reference compounds and fresh precipitates for each element were collected and analyzed for comparison to sediment spectra.

XANES spectra were used to identify oxidation states for chrominum and manganese and to qualitatively identify sediment components. Background-subtracted XANES spectra were normalized to maximum absorption and first-deriviative spectra were fit with linear combination of reference spectra using the program DATFIT (G. George, ref. 62). EXAFS spectra were quantitatively analyzed using EXAFSPAK[14] and FEFF[15] according to methods described in O'Day *et al.*[16] and Carroll *et al.*[17] Debye–Waller factors (σ^2) were fixed on values determined from fits to reference spectra of compounds of similar structure and composition to sediment components. For trace metals (Cd, Zn, Cr, Pb, and Mn), proportions of sulfide and oxide components in the sediment spectra were estimated based on the relative proportions of first-shell oxygen and sulfur backscatterers. For these spectra, detection of a unique bonding site is estimated at about 10–15 atom% of the total element signal. For iron, the sulfide and oxide components were quantitatively determined based on integrated areas of least-squares fits. Fit areas were calibrated using spectra of standard mixtures of pyrite (commercial), nontronite (The Clay Minerals Society, Standard NAu-1), and illite (The Clay Minerals Society, Standard IMt-1) in a ground quartz matrix at 5 atom% total iron to simulate sediment concentrations. Spectra of the reference mixtures were collected in fluorescence at room temperature at SSRL on beamlines 2-3 and 4-3. Based on sensitivity tests with known concentrations, the proportion of pyrite in these sediments can be determined to better than $\pm 5\%$ of the total iron in the sample (see ref. 18).

2.6. Geochemical modeling of porewaters

The aqueous geochemistry was modeled thermodynamically for sulfide, carbonate, oxide/hydroxide, and silicate saturation and aqueous complexation *versus* depth with the Geochemist's Workbench geochemical code[19] and SUPCRT92 database[20] modified to include aqueous Cd-, Cr-, Fe-, Mn-, Ni-, Pb, and Zn-sulfide species, and Zn-, Cd-, and Pb-carbonate and hydroxide phases (Table 1). Activity coefficients were calculated from the extended Debye–Hückel method, which is valid to ionic strengths of about 3 mol kg^{-1}. For these calculations, we used field temperature, porewater trace and major element concentrations with dissolved sulfur as HS^-, and sediment pH from core SC4. Alkalinity as HCO_3^- was calculated as a function of depth for core SC4 from a linear regression of the inorganic-carbon concentration measured in core SC2 data. For the surface sediments at 1.5 cm, alkalinity is calculated from measured pH and atmospheric CO_2, because the linear

Table 1 Thermodynamic equilibria and constants used in the geochemical modeling of the porewater chemistry in the Seaplane Lagoon sediments

	log K (25 °C)	Ref.
$Al(OH)_3$(gibbsite) + $3H^+ \rightarrow Al^{3+} + 3H_2O$	7.76	38
AlOOH(boehmite) + $3H^+ \rightarrow Al^{3+} + 2H_2O$	7.56	38
$CaCO_3$(calcite) $\rightarrow Ca^{2+} + CO_3^{2-}$	−8.48	39
$CaMg(CO_3)_2$(dolomite) $\rightarrow Ca^{2+} + Mg^{2+} + 2CO_3^{2-}$	−18.14	39
$CaSO_4 \cdot 2H_2O$(gypsum) $\rightarrow Ca^{2+} + SO_4^{2-} + 2H_2O$	−4.48	40
$Cd^{2+} + H_2O \rightarrow CdOH^+ + H^+$	−10.08	41
$Cd^{2+} + 2H_2O \rightarrow Cd(OH)_2^0 + 2H^+$	−20.34	41
$Cd^{2+} + 3H_2O \rightarrow Cd(OH)_3^{-1} + 3H^+$	−33.29	41
$Cd^{2+} + 4H_2O \rightarrow Cd(OH)_4^{2-} + 4H^+$	−47.33	41
$Cd^{2+} + Cl^- \rightarrow CdCl^+$	1.97	42
$Cd^{2+} + 2Cl^- \rightarrow CdCl_2$(aq)	2.59	42
$Cd^{2+} + 3Cl^- \rightarrow CdCl_3^-$	2.34	42
$Cd^{2+} + 4Cl^- \rightarrow CdCl_4^{2-}$	−1.46	42
$Cd^{2+} + CO_3^{2-} \rightarrow CdCO_3^0$	3.00	43
$Cd^{2+} + 2CO_3^{2-} \rightarrow Cd(CO_3)_2^{2-}$	6.40	43
$Cd^{2+} + CO_3^{2-} + H^+ \rightarrow CdHCO_3^+$	11.83	43
$Cd^{2+} + SO_4^{2-} \rightarrow CdSO_4^0$	−0.003	44
$CdHS^+ \rightarrow HS^- + Cd^{2+}$	−9.02	45[a]
$Cd(HS)_2 \rightarrow 2HS^- + Cd^{2+}$	−16.53	45[a]
$Cd(OH)_2$(beta) + $2H^+ \rightarrow Cd^{2+} + 2H_2O$	13.64	41
CdS + $H^+ \rightarrow HS^- + Cd^{2+}$	−15.91	44
$CdSO_4$(anglesite) $\rightarrow Cd^{2+} + SO_4^{2-}$	−0.11	44
$CdCO_3$(otavite) $\rightarrow Cd^{2+} + CO_3^{2-}$	−12.1	43
CdO(monteponite) + $2H^+ \rightarrow Cd^{2+} + H_2O$	15.1	46
$Cr^{3+} + Cl^- \rightarrow CrCl^{2+}$	7.60	47
$Cr^{3+} + 2Cl^- \rightarrow CrCl_2^-$	7.91	47
$CrHS^{2+} \rightarrow HS^- + Cr^{3+}$	−9.88	45[a]
CrS + $2H^+ + 0.25O_2$(aq) $\rightarrow 0.5H_2O +$ $Cr^{3+} + HS^-$	31.35	47
Cr_2O_3(eskolaite) + $6H^+ \rightarrow 3H_2O + 2Cr^{3+}$	7.64	44
$Cu^{2+} + Cl^- \rightarrow CuCl^+$	0.40	42
$Cu^{2+} + 2Cl^- \rightarrow CuCl_2$(aq)	−0.69	42
$Cu^{2+} + 3Cl^- \rightarrow CuCl_3^-$	−2.29	42
$Cu^{2+} + 4Cl^- \rightarrow CuCl_4^{2-}$	−4.94	42
CuS(covellite) + $H^+ \rightarrow HS^- + Cu^{2+}$	−22.83	39
$CuFeS_2$(chalcopyrite) + $2H^+ \rightarrow 2HS^- +$ $Fe^{2+} + Cu^{2+}$	−32.56	39
$Cu_2CO_3(OH)_2$(malachite) + $2H^+ \rightarrow 2H_2O +$ $CO_3^{2-} + 2Cu^{2+}$	−4.40	39
CuO(tenorite) + $2H^+ \rightarrow Cu^{2+} + H_2O$	7.66	39
$FeHS^+ \rightarrow HS^- + Fe^{2+}$	−5.52	48[a]
$(Fe)_2HS^{3+} \rightarrow HS^- + 2Fe^{2+}$	−10.02	48[a]
$(Fe)_3HS^{5+} \rightarrow HS^- + 3Fe^{2+}$	−15.30	48[a]
$Fe^{2+} + Cl^- \rightarrow FeCl^+$	−0.16	42
$Fe^{2+} + 2Cl^- \rightarrow FeCl_2$(aq)	−8.17	42
$Fe^{3+} + Cl^- \rightarrow FeCl^{2+}$	1.47	42
$Fe^{3+} + 2Cl^- \rightarrow FeCl_2^+$	2.13	49
$Fe^{3+} + 4Cl^- \rightarrow FeCl_4^-$	−0.79	49
FeS_2(pyrite) + $H_2O \rightarrow Fe^{2+} + 2HS^- +$ $0.5O_2$(aq)	−59.23	39
FeS(pyrrhotite) + $H^+ \rightarrow HS^- + Fe^{2+}$	−3.72	39
$FeCO_3$(siderite) $\rightarrow Fe^{2+} + CO_3^{2-}$	−10.52	39
FeOOH(goethite) + $2H^+ \rightarrow Fe^{2+} +$ $1.5H_2O + 0.25O_2$(aq)	−7.96	40
$Na_{0.33}Fe_2Al_{0.33}Si_{3.67}O_{10}(OH)_2$(Na-nontronite) + $5.32H^+ \rightarrow 2Fe^{2+} + 0.33Al^{3+} + O.5O_2$(aq) + $0.33Na^+ + 3.67SiO_2 + 3.66H_2O$	−28.51	50
$Mg_5Al_2Si_3O_{10}(OH)_8$ (7 Å chlorite) + $16H^+ \rightarrow 2Al^{3+} +$ $12H_2O + 3SiO_2$(aq) + $5Mg^{2+}$	70.61	39
$Mn^{2+} + Cl^- \rightarrow MnCl^+$	−0.14	42
$Mn^{2+} + 3Cl^- \rightarrow MnCl_3^-$	−0.77	44
$MnHS^+ \rightarrow HS^- + Mn^{2+}$	−5.00	48[a]
$(Mn)_2HS^{3+} \rightarrow HS^- + 2Mn^{2+}$	−9.55	48[a]
$(Mn)_3HS^{5+} \rightarrow HS^- + 3Mn^{2+}$	−13.63	48[a]
MnS(alabandite) + $H^+ \rightarrow HS^- + Mn^{2+}$	−0.05	39
$MnCO_3$(rhodochrosite) $\rightarrow Mn^{2+} + CO_3^{2-}$	−10.52	39
$Ni(OH)_2 + 2H^+ \rightarrow Ni^{2+} + 2H_2O$	7.64	44
$Ni^{2+} + Cl^- \rightarrow NiCl^+$	−1.00	42
$NiCO_3 \rightarrow CO_3^{2-} + Ni^{2+}$	–6.82	44
$NiHS^+ \rightarrow HS^- + Ni^{2+}$	−5.29	48[a]
$(Ni)_2HS^{3+} \rightarrow HS^- + 2Ni^{2+}$	−9.82	48[a]
$(Ni)_3HS^{5+} \rightarrow HS^- + 3Ni^{2+}$	−13.65	48[a]

Table 1 Thermodynamic equilibria and constants used in the geochemical modeling of the porewater chemistry in the Seaplane Lagoon sediments *(continued)*

	log K (25 °C)	Ref.
NiS_2(vaesite) + $H_2O \rightarrow Ni^{2+} + 2HS^- + 0.5O_2$(aq)	–61.34	39
NiS(millerite) + $H^+ \rightarrow HS^- + Ni^{2+}$	−8.03	51
PbS(galena) + $H^+ \rightarrow HS^- + Pb^{2+}$	−14.85	44
$Pb^{2+} + H_2O \rightarrow PbOH^+ + H^+$	−7.7	52
$Pb^{2+} + 2H_2O \rightarrow Pb(OH)_2 + 2H^+$	−17.09	52
$Pb^{2+} + 3H_2O \rightarrow Pb(OH)_3^- + 3H^+$	−28.09	52
$Pb^{2+} + Cl^- \rightarrow Pb\,Cl^+$	1.44	42
$Pb^{2+} + 2Cl^- \rightarrow PbCl_2$(aq)	2.00	42
$Pb^{2+} + 3Cl^- \rightarrow Pb\,Cl_3^-$	1.69	42
$Pb^{2+} + 4Cl^- \rightarrow Pb\,Cl_4^{2-}$	1.43	42
$Pb^{2+} + CO_3^{2-} \rightarrow PbCO_3$	6.58	53
$Pb^{2+} + 2CO_3^{2-} \rightarrow Pb(CO_3)^{2-}$	9.40	53
$PbCO_3$(cerussite) $\rightarrow Pb^{2+} + CO_3^{2-}$	−13.54	20
$Pb_3(CO_3)_2(OH)_2$(hydrocerussite) + $2H^+ \rightarrow 2CO_3^{2-} + 3Pb^{2+} + 2H_2O$	−18.81	52
$PbSO_4$(anglesite) $\rightarrow Pb^{2+} + SO_4^{2-}$	−7.85	39
$PbHS^+ \rightarrow HS^- + Pb^{2+}$	−8.62	45[a]
$Pb(HS)_2 \rightarrow 2HS^- + Pb^{2+}$	−16.43	45[a]
SiO_2(quartz) $\rightarrow SiO_2$(aq)	−4.0	39
SiO_2(α-cristobalite) $\rightarrow SiO_2$(aq)	−3.45	39
SiO_2(am. si.) $\rightarrow SiO_2$(aq)	−2.71	39
$Zn^{2+} + H_2O \rightarrow ZnOH^+ + H^+$	−8.96	54
$Zn^{2+} + 2H_2O \rightarrow Zn(OH)_2^0 + 2H^+$	−28.04	44
$Zn^{2+} + 3H_2O \rightarrow Zn(OH)_3^- + 3H^+$	−28.83	44
$Zn^{2+} + 4H_2O \rightarrow Zn(OH)_4^- + 4H^+$	−41.61	44
$Zn^{2+} + Cl^- \rightarrow ZnCl^+$	1.99	42
$Zn^{2+} + 2Cl^- \rightarrow ZnCl_2$(aq)	2.51	42
$Zn^{2+} + 3Cl^- \rightarrow ZnCl_3^-$	−0.02	42
$Zn^{2+} + CO_3^{2-} + H^+ \rightarrow ZnHCO_3^+$	8.91	54
$Zn^{2+} + CO_3^{2-} \rightarrow ZnCO_3^0$	3.9	55
$Zn^{2+} + SO_4^{2-} \rightarrow ZnSO_4^0$	−0.026	44
$Zn_2S_3^{2-} + 3H^+ \rightarrow 3HS^- + 2Zn^{2+}$	−1.07	56[a]
$Zn_4S_6^{4-} + 6H^+ \rightarrow 6HS^- + 4Zn^{2+}$	−5.22	56[a]
ZnS(sphalerite) + $H^+ \rightarrow HS^- + Zn^{2+}$	−11.44	39
$Zn(OH)_2(\beta) + 2H^+ \rightarrow Zn^{2+} + 2H_2O$	11.93	44
$Zn(OH)_2(\varepsilon) + 2H^+ \rightarrow Zn^{2+} + 2H_2O$	11.66	44
$Zn(OH)_2(\gamma) + 2H^+ \rightarrow Zn^{2+} + 2H_2O$	11.88	44
$ZnSO_4$(solid) $\rightarrow Zn^{2+} + SO_4^{2-}$	3.55	44
$ZnCO_3$(smithsonite) $\rightarrow Zn^{2+} + CO_3^{2-}$	−9.87	20
$Zn_5(OH)_6(CO_3)_2$ (hydrozincite) + $6H^+ \rightarrow 5Zn^{2+} + 2CO_3^{2-} + 6H_2O$	9.65	57

[a] Experimental values extrapolated to $I = 0$.

extrapolation yielded negative values. The solution was charge balanced by adjusting the chloride concentration.

3. Results

3.1 Depth profiles of the porewater chemistry

We report the porewater trace and major element, chloride, sulfur, and pH for core SC4 and the porewater total phosphorus, carbon, inorganic carbon, and organic carbon for core SC2 in Fig. 2 and in Tables 2 and 3. There are distinct trends in the porewater composition with depth in core SC4. Calcium, magnesium, potassium, sodium, chloride, and sulfide concentrations increase with depth to 25.5 cm and remain constant at greater depths. Aluminium concentrations are quite low and constant (with the exception of one outlying data point). Silica concentrations increase by about two times from surface sediments to a depth of 4.5 cm, and remain constant at greater depths. Iron concentrations were detected only at depths above 4.5 cm. Cadmium, chromium, and lead concentrations increase with depth following similar trends observed for their sediment concentrations. Nickel concentrations show a slight decrease with depth. Copper, manganese, and zinc depth profiles are more complicated. Manganese concentrations decrease to minimum at a depth of 4.5 cm, then increase to a maximum

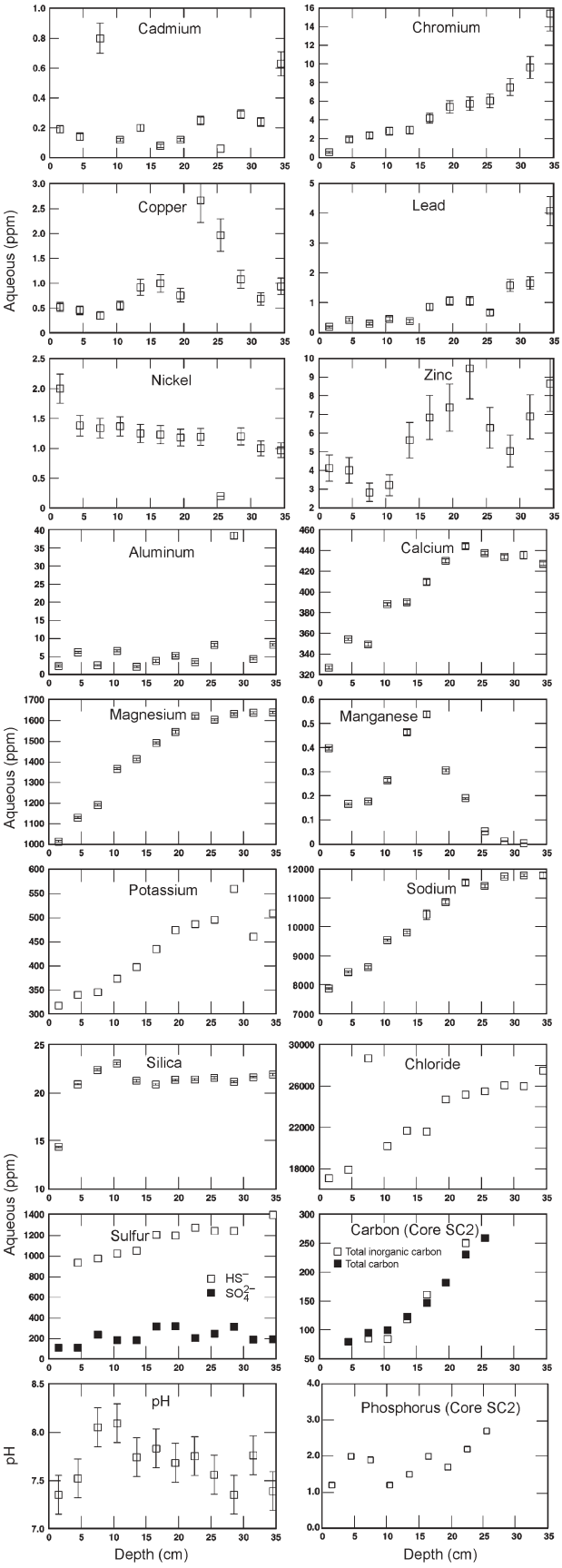

Fig. 2 Chemical composition of porewaters extracted from core SC4. Dissolved carbon data is from core SC2. Both cores were collected on July 10, 1997.

at a depth of 16.5 cm, and then decrease at greater depths. Zinc and copper concentrations increase to maximum at a depth of 22.5 cm, decrease between 22.5 and 28.5–31.5 cm, and

Table 2 Porewater trace- and major-elements extracted from Seaplane Lagoon core SC4 (July 10, 1998). Calcium, iron, potassium, magnesium, manganese, sodium, and silica were measured by ICP-AES. Aluminium, cadmium, chromium, copper, iron, lead, manganese, nickel, and zinc were measured by ICP-MS. Uncertainty for potassium was not reported

ICP-AES

Sample ID	Depth/cm	Ca (ppm)	Fe (ppm)	K (ppm)	Mg (ppm)	Mn (ppm)	Na (ppm)	Si (ppm)
SC4-1	1.5	327±1	2.20±0.01	318	1017±2	0.366±0.002	7870±20	14.4±0.0
SC4-2	4.5	355±1	0.20±0.01	340	1133±2	0.195±0.003	8440±20	20.9±0.0
SC4-3	7.5	350±2	<0.2	346	1192±2	0.182±0.004	8600±30	22.4±0.1
SC4-4	10.5	388±1	<0.2	374	1368±3	0.275±0.002	9540±20	23.0±0.1
SC4-5	13.5	390±1	<0.2	398	1414±4	0.375±0.001	9800±40	21.3±0.1
SC4-6	16.5	410±2	<0.2	435	1493±3	0.431±0.001	10400±200	20.9±0.0
SC4-7	19.5	430±2	<0.2	474	1546±5	0.271±0.002	10900±100	21.3±0.1
SC4-8	22.5	444±2	0.69±0.00	487	1620±6	0.173±0.001	11500±100	21.4±0.1
SC4-9	25.5	438±1	<0.2	496	1604±4	<0.1	11400±100	21.6±0.1
SC4-10	28.5	434±2	<0.2	560	1633±4	<0.1	11700±0	21.2±0.1
SC4-11	31.5	436±3	<0.2	461	1639±3	<0.1	11800±0	21.7±0.0
SC4-12	34.5	427±2	<0.2	509	1640±5	<0.1	11800±100	21.9±0.1

ICP-MS

Sample ID	Depth/cm	Al (ppb)	Cd (ppb)	Cr (ppb)	Cu (ppb)	Fe (ppb)	Mn (ppb)	Ni (ppb)	Pb (ppb)	Zn (ppb)
SC4-1	1.5	2.4±0.2	0.19±0.02	0.53±0.06	0.52±0.09	3000±60	395±4.0	2.00±0.24	0.19±0.02	4.12±0.70
SC4-2	4.5	6.2±0.1	0.14±0.02	1.89±0.23	0.46±0.08	1400±70	165±1.7	1.38±0.17	0.43±0.05	4.00±0.68
SC4-3	7.5	2.6±0.1	0.80±0.10	2.35±0.28	0.35±0.06	1000±70	175±3.5	1.34±0.16	0.30±0.04	2.82±0.48
SC4-4	10.5	6.6±0.1	0.12±0.01	2.80±0.34	0.55±0.09	500±25	263±5.3	1.37±0.16	0.46±0.06	3.21±0.55
SC4-5	13.5	2.2±0.1	0.20±0.02	2.91±0.35	0.92±0.16	<110	462±9.2	1.25±0.15	0.38±0.05	5.61±0.95
SC4-6	16.5	3.8±0.3	0.08±0.01	4.19±0.50	1.00±0.17	<110	536±10.7	1.23±0.15	0.86±0.10	6.83±1.16
SC4-7	19.5	5.3±0.2	0.12±0.01	5.40±0.65	0.76±0.13	<110	304±3.0	1.18±0.14	1.06±0.13	7.36±1.25
SC4-8	22.5	3.5±0.2	0.25±0.03	5.74±0.69	2.67±0.45	<110	188±1.9	1.19±0.14	1.05±0.13	9.45±1.61
SC4-9	25.5	8.2±0.3	<0.06	6.04±0.72	1.97±0.33	<110	52±0.5	<0.2	0.67±0.08	6.28±1.07
SC4-10	28.5	38.4±0.8	0.29±0.03	7.51±0.90	1.08±0.18	<110	10±0.3	1.20±0.14	1.58±0.19	5.04±0.86
SC4-11	31.5	4.4±0.2	0.24±0.03	9.61±1.15	0.69±0.12	<110	2±0.1	1.00±0.12	1.65±0.20	6.88±1.17
SC4-12	34.5	8.3±0.2	0.63±0.08	15.38±1.85	0.94±0.16	<110	<1	0.97±0.12	4.07±0.49	8.64±1.47

Table 3 Porewater concentrations of total P, total carbon (TC), total inorganic carbon (TIC), and total organic carbon (TOC), total S, Cl- and pH from Seaplane Lagoon cores collected on July 10, 1998 (na = not analyzed)

Core SC2

Sample ID	Depth/cm	P (ppm)	TC (ppm)	TIC (ppm)	TOC (ppm)
SC2-0		0.5	na	na	na
SC2-1	1.5	1.2	na	na	na
SC2-2	4.5	2.0	80	na	<14
SC2-3	7.5	1.9	95	86	<14
SC2-4	10.5	1.2	100	84	18
SC2-5	13.5	1.5	123	119	17
SC2-6	16.5	2.0	147	161	<14
SC2-7	19.5	1.7	182	na	na
SC2-8	22.5	2.2	230	250	<14
SC2-9	25.5	2.7	259	na	na

Core SC4

Sample ID	Depth/cm	S (ppm)	Cl^- (ppt)	pH
SC4-1	1.5	686	17.1	7.35
SC4-2	4.5	736	17.9	7.52
SC4-3	7.5	759	28.7	8.05
SC4-4	10.5	859	20.2	8.09
SC4-5	13.5	893	21.7	7.74
SC4-6	16.5	949	21.6	7.83
SC4-7	19.5	976	24.7	7.68
SC4-8	22.5	996	25.2	7.75
SC4-9	25.5	952	25.5	7.56
SC4-10	28.5	955	26.1	7.35
SC4-11	31.5	1036	26.0	7.76
SC4-12	34.5	1021	27.5	7.39

increase at greater depths. In core SC2, total dissolved total inorganic carbon and total phosphorus concentrations increase with depth.

The dissolved major metal concentrations are close to the equilibrium solubility of common soil minerals (Table 4). Dissolved silica concentrations are close to saturation with respect to β-cristobalite, a quartz polymorph, but supersaturated with respect to quartz. The dissolved aluminium concentrations are close to saturation with respect to gibbsite, ($Al(OH)_3$) and not 7 Å chlorite (micaceous clay) which was identified in the X-ray diffraction analysis of the sediments. The dissolved calcium concentrations are undersaturated with respect to calcite ($CaCO_3$) in the surface sediments (1.5 cm), but supersaturated at greater depths. Apatite ($Ca_5OH(PO_4)_3$) is supersaturated through out the core. In the top 5 cm, dissolved iron concentrations are supersaturated with respect to sulfide phases, and at greater depths, iron concentrations are below detection.

Dissolved trace element concentrations are not exclusively controlled by the solubility of sulfide phases when aqueous complexation by HS^- and S^{2-} is included (Table 4). Of the seven trace elements measured, only cadmium and lead concentrations appear to be limited by the solubility of CdS(s) and galena (PbS). Zinc and nickel concentrations are supersaturated with respect to sphalerite (ZnS) and millerite (NiS) by 2–4 orders of magnitude, and manganese and chromium concentrations are undersaturated with respect to alabandnite (MnS) and CrS (we do not have thermodynamic data for Cr_2S_3). The high covellite (CuS) saturation indices (log SI 7–8) may reflect the absence of known formation constants for aqueous copper HS^- and S^{2-} complexes. With the exception of chromium, the stability of trace element HS^- and S^{2-} complexes yields porewaters that are significantly undersaturated with respect to carbonates or hydroxides. Cadmium, copper, lead, nickel, and zinc are all undersaturated with respect to otavite ($CdCO_3$) and $Cd(OH)_2$, malachite ($Cu_2CO_3(OH)_2$), tenorite (CuO), cerussite ($PbCO_3$), $NiCO_3$ and $Ni(OH)_2$, rhodochrosite ($MnCO_3$) and $Mn(OH)_2$, and smithsonite ($ZnCO_3$), and β-$Zn(OH)_2$. Dissolved chromium concentrations are

Table 4 Porewater water chemistry from Seaplane Lagoon, Alameda NAS compared with sulfide, carbonate, phosphate, silicate, oxide, and hydroxide minerals reported as the saturation index at 25 °C (log SI). Calculations used trace and major elements; sulfide and sulfate are from core SC4 and total inorganic carbon is from core SC2

Sulfides

Sample ID	Depth/cm	CdS	CrS	CuS covellite	$CuFeS_2$ chalcopyrite	FeS_2 pyrite	FeS pyrrhotite	MnS alabandite	NiS millerite	PbS galena	ZnS sphalerite
SC4-1	1.5	−0.1	−16.2	7.4	14.4	8.9	1.0	−3.0	2.4	−1.3	4.0
SC4-2	4.5	−0.1	−15.1	7.5	14.0	9.1	0.9	−3.2	2.5	−0.8	3.9
SC4-3	7.5	1.2	−15.0	7.3				−2.7	3.0	−0.4	3.56
SC4-4	10.5	0.6	−13.8	10.9				−2.5	3.0	−0.1	3.6
SC4-5	13.5	0.2	−15.1	7.9				−2.6	5.6	2.2	5.0
SC4-6	16.5	−0.2	−14.9	8.1				−2.4	2.7	−0.4	3.8
SC4-7	19.5	−0.1	−15.0	7.7				−2.8	2.5	−0.4	3.9
SC4-8	22.5	0.2	−14.9	8.3				−3.0	2.6	−0.4	3.9
SC4-9	25.5		−15.0	7.9				−3.7		−0.7	3.9
SC4-10	28.5	0.0	−15.2	7.3				−4.6	2.2	−0.5	4.0
SC4-11	31.5	0.6	−14.6	7.7				−4.9	2.6	−0.2	3.8
SC4-12	34.5	0.6	−14.4	7.7					2.5	0.2	3.8

Carbonates

Sample ID	Depth/cm	$CaCO_3$ calcite	$CdCO_3$ otavite	$Cu_2CO_3(OH)_2$ malachite	$FeCO_3$ siderite	$MnCO_3$ rhodochrosite	$NiCO_3$	$PbCO_3$ cerussite	$ZnCO_3$ smithsonite
SC4-1	1.5	−1.1	−16.2	−29.5	−4.5	−5.2	−11.1	−14.9	−9.9
SC4-2	4.5	−0.8	−16.1	−29.0	−4.5	−5.3	−11.0	−14.4	−9.9
SC4-3	7.5	0.9	−13.5	−27.7		−3.5	−9.2	−12.6	−8.9
SC4-4	10.5	1.1	−14.0	−20.2		−3.1	−9.0	−12.2	−8.7
SC4-5	13.5	0.8	−14.7	−26.9		−3.5	−6.6	−10.1	−7.6
SC4-6	16.5	1.0	−14.9	−26.5		−3.2	-.95	−12.6	−8.8
SC4-7	19.5	0.9	−14.8	−27.4		−3.6	−9.6	−12.6	−8.6
SC4-8	22.5	1.1	−14.4	−26.1		−3.6	−9.4	−12.5	−8.5
SC4-9	25.5	0.9		−27.0		−4.3		−12.8	−8.5
SC4-10	28.5	−0.5	−15.8	−29.4		−6.4	−10.9	−13.8	−9.6
SC4-11	31.5	1.3	−13.8	−27.1		−5.4	−9.3	−12.1	−8.4
SC4-12	34.5	1.3	−13.7	−26.9			−9.2	−11.6	−8.3

Silicates

Sample ID	Depth/cm	$PbHPO_4$	$Ca_5OH(PO_4)_3$ apatite	$Pb_5PO_4Cl_3$ pyromorphite	β-$Zn(OH)_2$	SiO_2 quartz	SiO_2 β-cristobalite	$Mg_5Al_2Si_3O_{10}(OH)_8$ 7A-chlorite
SC4-1	1.5	−11.6	1.8	−55.5	−10.1	0.7	−0.3	−0.1
SC4-2	4.5	−11.4	2.5	−53.9	−10.1	0.8	0.2	2.8
SC4-3	7.5	−11.2	4.6	−51.8	−9.8	0.6	−0.4	5.5
SC4-4	10.5	−10.9	5.1	−50.3	−9.6	0.7	−0.3	7.2
SC4-5	13.5	−8.6	3.5	−39.5	−8.9	0.8	−0.2	3.8
SC4-6	16.5	−11.2	4.3	−52.5	−10.1	0.7	−0.3	5.1
SC4-7	19.5	−11.2	3.5	−52.6	−10.1	0.8	−0.2	4.3
SC4-8	22.5	−11.2	4.1	−52.6	−10.1	0.8	−0.2	4.5
SC4-9	25.5	−11.5	3.6	−52.3	−10.2	0.8	−0.2	3.8
SC4-10	28.5	−10.7	2.8	−53.1	−10.3	0.8	−0.2	3.6
SC4-11	31.5	−10.9	4.3	−51.5	−10.2	0.8	−0.2	4.7
SC4-12	34.5	−10.5	4.2	−51.2	−10.1	0.8	−0.3	5.2

Table 4 Porewater water chemistry from Seaplane Lagoon, Alameda NAS compared with sulfide, carbonate, phosphate, silicate, oxide, and hydroxide minerals reported as the saturation index at 25 °C (log SI). Calculations used trace and major elements; sulfide and sulfate are from core SC4 and total inorganic carbon is from core SC2 *(continued)*

Oxides/hydroxides/phosphates																		
Sample ID	Depth/ cm	$Al(OH)_3$ gibbsite	$Cd(OH)_2$	Cr_2O_3 eskolaite	CuO tenorite	$Fe(OH)_2$	FeOOH goethite	$Ni(OH)_2$	$Mn(OH)_2$	$MnHPO_4$	$Pb_3(PO_4)_2$	$Ni_3(PO_4)_2$	$Mn_3(PO_4)_2$	$Cd_3(PO_4)_2$	$Cu_3(PO_4)_2$	$Zn_3(PO_4)_2 \cdot 4H_2O$ hopeite	$FePO_4 \cdot 2H_2O$ strengite	$FeCr_2O_4$ chromite	$MgCr_2O_4$ magnesio-chromite
SC4-1	1.5	0.6	−20.4	−1.0	−13.8	−7.3	−4.6	−9.1	−9.4	−1.2	−41.4	23.1	−22.7	−53.0	−47.0	−24.6	−13.2	8.3	4.8
SC4-2	4.5	0.9	−20.4	1.8	−13.6	−7.3	−4.4	−8.9	−9.5	−1.6	−40.8	−23.5	−23.8	−53.5	−47.1	−25.4	−13.4	0.9	0.9
SC4-3	7.5	0.0	−18.4	4.3	−13.2			−7.8	−8.4	−1.4	−39.2	−22.0	−22.2	−49.5	−47.9	−26.5			4.4
SC4-4	10.5	0.3	−19.0	7.0	−9.5			−7.7	−8.1	−1.2	−38.2	−21.8	−21.4	−51.5	−37.0	−26.1			7.2
SC4-5	13.5	0.2	−20.0	2.3	−13.1			−5.7	−8.8	−1.3	−32.6	−14.6	−22.3	−53.3	−46.4	−22.6			2.0
SC4-6	16.5	0.4	−20.3	3.1	−12.8			−8.5	−8.6	−1.2	−39.6	−23.2	−21.9	−54.3	−45.9	−26.3			3.0
SC4-7	19.5	0.7	−20.4	5.4	−13.4			−8.8	−9.1	−1.5	−39.7	−23.7	−23.0	−54.2	−47.2	−26.0			5.0
SC4-8	22.5	0.4	−20.0	2.8	−12.8			−8.7	−9.2	−1.6	−39.5	−23.5	−23.4	−53.0	−45.3	−26.0			2.5
SC4-9	25.5	1.0		1.8	−13.3				−10.1	−2.0	−40.0		−25.1		−45.9	−25.3			1.1
SC4-10	28.5	1.8	−20.5	0.8	−14.0			−9.4	−11.2	−2.7	−39.1	−23.8	−27.5	−52.9	−47.2	−24.8			−0.3
SC4-11	31.5	0.5	−19.6	3.3	−13.4			−8.8	−11.2	−3.5	−38.8	−23.5	−29.1	−51.7	−47.0	−26.1			3.0
SC4-12	34.5	0.8	−19.6	3.7	−13.3			−8.8			−37.6	−23.6		−51.6	−46.8	−25.9			3.4

1 to 6 orders-of-magnitude higher than eskolaite (Cr_2O_3) and magnesiochromite ($MgCrO_4$) saturation. Manganese is the only trace metal that may be controlled by phosphate mineral solubility, with concentrations that are slightly undersaturated with respect to $MnHPO_4$(s).

3.2 Depth profiles of the bulk sediment chemistry and mineralogy

The depth profiles of cadmium, chromium, cobalt, copper, iron, lead, manganese, nickel, sulfur and zinc for the cores are shown in Fig. 3 and tabulated in Table 5. The chemical composition of the sediments with depth is quite uniform in the six cores. In the undisturbed 0.5 m push cores, cadmium, chromium, copper, lead, mercury, and zinc concentrations increase from low values in the surface sediments to higher values at depths greater than 20 to 30 cm below the sediment–water surface. The concentrations range from 10 to 350 μg g^{-1} for cadmium, from 230 to 1150 μg g^{-1} for chromium, from 100 to 240 μg g^{-1} for copper, from 180 to 1400 μg g^{-1} for lead, from 110 to 180 μg g^{-1} for nickel, and from 240 to 630 μg g^{-1} for zinc. Cobalt concentrations are low and vary between 14 and 30 μg g^{-1}, with peak concentrations at depths of 20 to 45 cm as high as 160 μg g^{-1}. Manganese concentrations are constant with depth and are about 450 μg g^{-1}. Iron concentrations increase from about 4.5 wt% in the surface sediments to about 5.5 wt% at depths greater than 10 cm. Sulfur concentrations increase from 1 wt% in the surface sediments to about 2 wt% at depths of 30 to 40 cm. Gravity cores sampled the sediments to greater depth (1 m) than the push cores, and show that the trace metals concentrations continue to increase to about 80 cm (Table 5). At greater depths the concentrations drop to very low levels comparable to the pristine levels in San Francisco Bay.[21]

No trends in sediment mineralogy were observed as a function of depth. The sediments are primarily quartz with about 10 to 15 wt% phyllosilicate minerals. There is no difference in the bulk mineralogy as a function of depth. Minerals identified in XRD patterns are 80–90% quartz, and a minimum of 2 wt% hornblende, mica, chlorite, smectite, illite, and pyrite.

3.3 Depth profiles of metal bonding from XAS analysis

Analyses of EXAFS and XANES spectra were used to determine the dominant local coordination environment of individual metals in the sediments. In bulk samples, the absorption signal is an average of all coordination environments of a particular element. Although absorption spectra were collected on samples with porewater present, the XAS signal is dominated by sites associated with solid phases because metal concentrations are roughly three orders-of-magnitude higher in the solids than in the associated porewater. Ligands in the first coordination shell were identified as either sulfur or oxygen. Quantitative analysis of EXAFS spectra was used to estimate the relative amount of ligation by sulfur (as sulfide) or oxygen atoms, or as a mixture of both atoms. Qualitative comparisons and linear combinations of XANES spectra of reference compounds were used to determine dominant components in the sediment samples for elements for which good quality EXAFS spectra could not be obtained.

3.3.1 Sulfide-associated metals. X-ray absorption spectra for cadmium from two sediment samples show that cadmium is bonded only by first-neighbor sulfur atoms (Fig. 4a). There is no evidence in the EXAFS spectra for coordination by oxygen, which would be evident by a shift to a shorter first-shell distance characteristic of Cd–O bond lengths. There is also no evidence for backscattering from atoms beyond the first

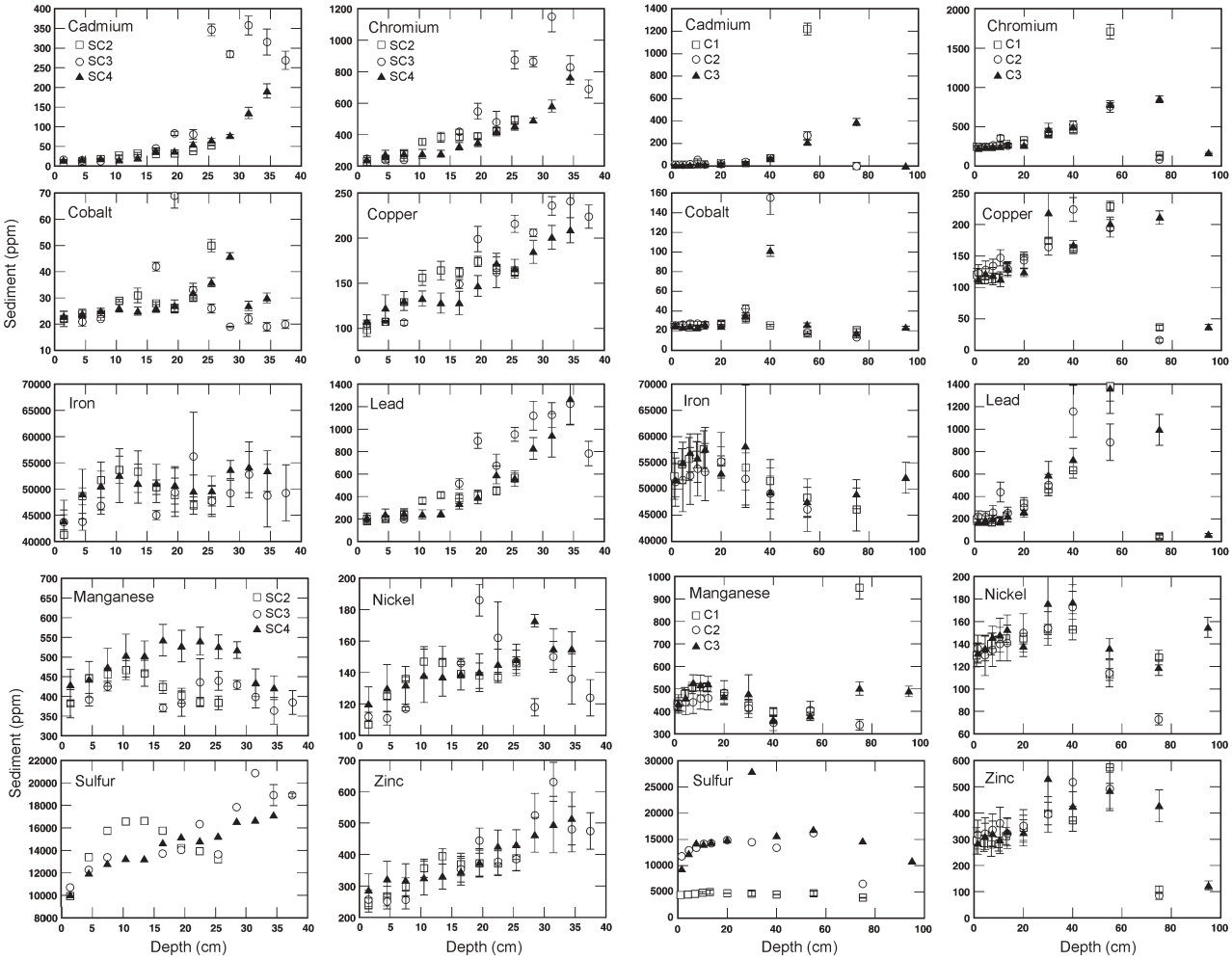

Fig. 3 Chemical composition of Seaplane Lagoon sediments from cores SC2, SC3, SC4 (left hand columns), C1, C2, and C3 (right hand columns).

coordination shell. Sediment spectra are identical to those of two freshly precipitated cadmium sulfide samples, which are the same regardless of whether or not iron was present in the reactant solution. First coordination shell Cd–S interatomic distances determined from least-squares fits are similar to those of crystalline CdS (Table 6), consistent with coordination in a sulfide phase (for which $N_{Cd–S} = 4$). The lack of atomic backscattering beyond the sulfur coordination shell for both the natural sediments and the reference laboratory precipitates indicates that the cadmium sulfide phase is highly disordered on a local atomic scale. Although the total cadmium concentrations differ significantly between the sample at 34.5 cm (192 μg g^{-1}Cd) and at 55.0 cm (1222 μg g^{-1}Cd), the local coordination determined by EXAFS analysis is identical.

Analyses of zinc EXAFS spectra indicate that zinc is dominantly coordinated in a sulfide phase in the sediments, with a secondary fraction of zinc associated with an oxide component (Fig. 4b). Interatomic distances derived from fits indicate that the sulfide component is locally identical to that of sphalerite (ZnS, for which first coordination shell $N_{Zn–S} = 4$) (Table 6). However, the much lower peak amplitudes in the Fourier transforms of the sediment samples spectra compared to those of crystalline sphalerite show that backscattering from zinc and sulfur atoms beyond the first sulfur shell is weak. This indicates formation of a poorly crystalline sulfide phase and/or small particle size. For the oxide component, zinc EXAFS spectra do not correspond to a single zinc oxide phase. Zinc occurs in oxide and silicate compounds in both octahedral and tetrahedral coordination. First coordination shell least-squares fits gave average Zn–O distances that were variable but consistent with dominantly octahedral coordination of zinc (Table 6). Analyses of the scattering from second neighbor Zn–Me atoms (where Me is a metal cation) gave interatomic distances indicative of edge sharing of octahedra ($R_{Zn–Me}$ = 3.06–3.13 Å), and of corner sharing of octahedra and/or tetrahedra ($R_{Zn–Me}$ = 3.21–3.37 Å). Because the backscattering functions overlap one another in this range of interatomic distances, the spectra could not be uniquely fit by a single element for each atomic shell. The closer Zn–Me shell could be fit with a combination of iron (or similar Z transition metal), magnesium, or aluminium. The more distant Zn–Me shell could be fit with iron, aluminium, or silicon. These observations suggest zinc substitution in one or more silicate or oxide phases. Given that phyllosilicate minerals comprise about 10–15 wt% of the bulk sample, it is likely that some zinc is present in these minerals. Substitution of zinc into the octahedral sites of clay minerals or micas is consistent with the interatomic distances determined for the oxide component. Substitution of small amounts of zinc into other oxide phases such as magnetite cannot be determined from these data.

The relative atomic proportions of zinc sulfide and oxide components in the sediments were estimated from fits to Fourier-filtered first coordination shell EXAFS spectra. Zinc was assumed to be tetrahedrally coordinated by sulfur in the sulfide component and octahedrally coordinated by oxygen in the oxide component. In fits to the total EXAFS spectra, interatomic distances and coordination numbers (N) for zinc and sulfur shells were fixed on crystallographic values for sphalerite (Table 6), with N scaled to the proportion of sulfide component determined in the first coordination shell fit. Using this approach, there is little change in the relative proportions of sulfide and oxide components as a function of depth in core

Table 5 Bulk sediment chemistry from Seaplane Lagoon cores SC2, SC3, SC4, C1, C2 and C3 reported as the average (± uncertainty) of 2–4 replicate analyses multiplied by 1.47 to correct for solution viscosity

Core SC2

Sample ID	Depth/cm	Al (ppm)	Ca (ppm)	Cd (ppm)	Co (ppm)	Cr (ppm)	Cu (ppm)	Fe (ppm)	Mg (ppm)	Mn (ppm)	Ni (ppm)	Pb (ppm)	S (ppm)	Zn (ppm)
SC2-1	1.5	41700±4900	11000±900	11.0±2.0	22.2±2.9	230±24	98±7	41300±4700	7350	382±36	108±12	183±21	9950	240±22
SC2-2	4.5	45300±4200	9840±200	12.7±0.4	24.6±0.1	248±7	108±2	48700±1600	9180	447±8	125±2	200±21	13400	268±31
SC2-3	7.5	46300±4000	8510±330	18.8±0.2	24.7±0.8	284±14	129±3	51800±1700	9840	456±17	136±1	240±43	15800	298±28
SC2-4	10.5	49000±3400	8820±410	28.1±1.8	29.3±0.5	355±21	157±8	53700±2600	10300	467±24	148±9	365±27	16600	357±29
SC2-5	13.5	48400±3900	8730±530	32.7±2.9	31.0±2.8	385±32	164±11	53400±3900	10300	459±33	147±11	415±28	16600	395±25
SC2-6	16.5	45100±3200	8510±410	30.4±0.8	28.1±0.5	386±20	163±5	50400±1400	9890	424±16	139±2	387±46	15800	369±36
SC2-7	19.5	45500±4800	20900±600	33.1±1.9	26.91.7±	392±20	174±6	49000±3200	9440	402±19	138±8	414±44	14200	373±41
SC2-8	22.5	44200±4000	7770±210	38.9±0.9	30.2±1.1	425±18	168±4	47000±1600	9400	386±12	137±3	453±36	13900	373±39
SC2-9	25.5	45800±4300	8040±220	53.4±1.1	50.6±2.4	494±27	163±5	48000±2800	9790	384±17	146±4	568±42	13200	389±39

Core SC3

Sample ID	Depth/cm	Al (ppm)	Ca (ppm)	Cd (ppm)	Co (ppm)	Cr (ppm)	Cu (ppm)	Fe (ppm)	Mg (ppm)	Mn (ppm)	Ni (ppm)	Pb (ppm)	S (ppm)	Zn (ppm)
SC3-1	1.5	41600±4300	9280±216	17±1	23±0	248±8	106±4	43700±1400	9420±2910	384±7	112±3	210±26	10700	257±30
SC3-2	4.5	42800±3800	10300±428	16±1	21±2	240±12	107±1	43800±1600	10100±2900	392±16	112±4	210±6	12300	251±23
SC3-3	7.5	42900±4500	13200±289	13±0	27±1	242±8	107±3	46800±1600	10900±3300	425±11	117±1	199±15	13400	256±29
SC3-6	16.5	41100±3400	10100±387	46±1	43±2	419±16	149±5	45100±900	11100±3400	371±10	147±1	516±47	13700	354±41
SC3-7	19.5	44500±5100	9110±555	84±5	69±5	550±51	199±14	49400±4600	12300±3300	382±32	186±10	898±70	14100	445±40
SC3-8	22.5	45800±6600	9330±1100	81±12	33±3	481±68	162±17	56200±8400	13400±3500	436±60	163±23	676±103	16400	377±40
SC3-9	25.5	33500±3100	10000±335	347±14	26±2	876±57	216±9	47700±2900	12400±3600	440±24	147±7	955±63	13700	386±38
SC3-10	28.5	38200±4300	9970±45	285±8	20±0	865±33	207±4	49200±2500	12500±4000	429±12	119±6	1120±129	17800	525±70
SC3-11	31.5	37400±4000	11200±573	358±24	22±2	1150±100	236±10	52800±4400	12400±3500	399±28	150±10	1130±111	20900	631±62
SC3-12	34.5	34600±5100	14100±1110	316±33	19±2	830±74	241±18	48800±6000	11100±3600	364±34	137±16	1230±188	18900	481±72
SC3-13	37.5	35400±4900	10400±660	270±23	20±2	691±57	226±13	49300±5300	11400±3400	385±30	125±12	784±108	18900	475±58

Core SC4

Sample ID	Depth/cm	Al (ppm)	Ca (ppm)	Cd (ppm)	Co (ppm)	Cr (ppm)	Cu (ppm)	Fe (ppm)	Mg (ppm)	Mn (ppm)	Ni (ppm)	Pb (ppm)	S (ppm)	Zn (ppm)
SC4-1	1.5	44300±6100	11200±1100	15±2	24±2	243±23	108±8	44000±3900	11900±3400	429±40	120±11	214±40	10100	287±52
SC4-2	4.5	46900±6500	9800±1100	17±2	25±2	275±27	123±15	49100±4700	13600±3700	443±46	130±15	242±49	12000	322±57
SC4-3	7.5	47100±6100	9700±1100	19±2	25±1	278±28	131±10	50700±4600	14000±3600	474±48	132±12	249±45	12800	318±53
SC4-4	10.5	48300±6100	10200±1200	15±2	26±1	279±29	133±8	52600±5100	14700±3600	504±54	138±17	242±42	13300	326±54
SC4-5	13.5	48900±4900	10300±900	21±2	26±2	280±21	128±11	51100±3700	15900±3100	503±38	137±12	251±33	13200	331±40
SC4-6	16.5	48500±4800	10600±900	39±3	27±2	327±24	129±13	51100±3600	15800±3200	543±40	139±10	338±47	14700	346±43
SC4-7	19.5	47800±4600	9200±800	38±3	28±2	351±26	148±12	50800±3600	15900±3200	528±40	140±12	393±55	15200	374±45
SC4-8	22.5	46800±4600	9700±700	56±5	33±2	422±27	172±11	49600±3100	15600±3200	541±35	145±10	593±79	14900	426±52
SC4-9	25.5	46900±4300	8900±600	66±5	36±2	456±26	166±11	49700±2800	15700±3100	526±30	148±10	562±69	15300	432±47
SC4-10	28.5	48200±4900	9600±300	78±3	47±1	493±15	189±13	53800±1800	15400±3800	518±21	173±4	831±97	16600	463±55
SC4-11	31.5	44700±7000	14800±1300	136±14	27±2	584±38	202±13	54200±4800	14900±4700	435±35	155±13	946±192	16700	496±90
SC4-12	34.5	46200±6200	10600±700	192±18	31±2	766±45	210±14	53500±3900	15200±4300	42230±	155±11	1270±230	17100	515±84

Table 5 Bulk sediment chemistry from Seaplane Lagoon cores SC2, SC3, SC4, C1, C2 and C3 reported as the average (± uncertainty) of 2–4 replicate analyses multiplied by 1.47 to correct for solution viscosity *(continued)*

Core C1

Sample ID	Depth/cm	Al (ppm)	Ca (ppm)	Cd (ppm)	Co (ppm)	Cr (ppm)	Cu (ppm)	Fe (ppm)	Mg (ppm)	Mn (ppm)	Ni (ppm)	Pb (ppm)	S (ppm)	Zn (ppm)
C1-1	75.0	34700±4400	9460±350	1±0	22±2	159±9	40±4	46100±4100	9670±2940	952±51	129±7	57±24	3940±80	108±14
C1-2	55.0	32000±3800	21900±600	1220±50	19±1	1730±90	232±8	48400±3600	12300±3500	400±18	113±5	1400±140	4770±480	574±61
C1-3	40.0	41800±5200	8680±260	72±4	27±1	470±26	165±7	51600±4100	13200±3800	398±20	1530±10	645±69	4550±60	373±42
C1-4	30.0	44600±5000	8950±330	29±1	34±2	424±25	177±6	54100±4300	13200±3800	427±23	153±5	475±53	4740±480	399±43
C1-5	20.0	46500±4800	8810±200	30±2	28±2	346±4	150±4	55100±3000	13200±4200	479±6	145±5	347±55	4790±50	344±48
C1-6	13.5	48300±4800	8930±190	20±1	27±1	300±11	137±3	57600±3500	13900±3900	508±19	145±3	241±27	5000±400	313±33
C1-7	10.5	47800±4100	8860±200	15±1	25±1	271±11	118±7	56600±2500	13700±3800	508±17	144±3	195±24	4900±190	282±27
C1-8	7.5	48500±6400	10000±330	14±1	25±1	262±12	116±6	55800±4100	14200±4700	505±25	140±10	185±37	4700	280±44
C1-9	4.5	48200±4600	9400±290	11±2	27±1	259±16	116±7	54700±3000	13900±4000	478±29	133±1	188±21	4590	285±31
C1-10	1.5	47000±6100	9210±350	15±1	26±2	264±9	123±10	52600±4500	13600±4600	430±23	131±10	206±45	4460	295±51

Core C2

Sample ID	Depth/cm	Al (ppm)	Ca (ppm)	Cd (ppm)	Co (ppm)	Cr (ppm)	Cu (ppm)	Fe (ppm)	Mg (ppm)	Mn (ppm)	Ni (ppm)	Pb (ppm)	S (ppm)	Zn (ppm)
C2-1	1.5	44100±6000	9280±970	15±1	27±2	265±24	126±13	51400±4600	14700±4000	434±41	136±12	234±49	11800	318±55
C2-2	4.5	43800±6500	9690±1320	13±2	27±3	264±32	131±14	51700±6000	14700±4000	442±56	130±18	231±49	13000	322±61
C2-3	7.5	43800±6200	8680±1030	18±2	28±3	281±30	137±11	52600±5400	14500±4000	441±49	135±15	269±64	13500	336±61
C2-4	10.5	45000±6200	9170±1060	58±7	28±2	373±37	150±13	53900±5100	15500±4100	458±47	140±15	451±89	14200	361±62
C2-5	13.5	46100±6500	9120±1100	16±2	27±3	278±29	132±12	53300±5400	15100±4000	460±52	141±16	266±52	14300	322±57
C2-6	20.0	48400±6900	9150±1120	20±3	28±3	309±33	146±13	55300±5500	16200±4300	484±53	150±17	313±67	14900	351±62
C2-7	30.0	45000±6100	9180±1040	40±4	44±4	455±44	167±13	52000±5000	15800±4200	414±41	154±15	514±96	14500	395±68
C2-8	40.0	36000±4900	9440±1020	73±10	157±17	544±51	227±19	49200±4900	14800±4000	350±35	173±20	1169±231	13500	518±92
C2-9	55.0	33400±4300	12200±1300	274±40	20±1	774±73	197±14	46200±4200	13500±3500	406±38	114±12	895±162	16300	492±82
C2-10	75.0	31200±3700	12300±800	1±0	14±1	100±6	19±3	23300±1600	6550±1800	341±24	73±5	55±13	6570	85±14

Core C3

Sample ID	Depth/cm	Al (ppm)	Ca (ppm)	Cd (ppm)	Co (ppm)	Cr (ppm)	Cu (ppm)	Fe (ppm)	Mg (ppm)	Mn (ppm)	Ni (ppm)	Pb (ppm)	S (ppm)	Zn (ppm)
C3-1	1.5	46300±5600	9580±580	8±1	26±1	238±14	115±6	51700±3100	15000±4000	434±28	132±9	182±29	9460	285±42
C3-2	4.5	47900±6200	10700±800	10±1	25±1	252±16	124±9	55000±3900	15900±4300	461±35	136±11	201±39	12300	311±50
C3-3	7.5	50600±6100	9320±630	10±1	26±2	264±16	121±14	56900±3600	16600±4400	528±36	146±10	209±38	14300	321±49
C3-4	10.5	49200±6700	9400±830	10±1	24±3	262±20	117±12	55900±4600	16400±4600	518±44	148±15	196±40	14100	297±51
C3-5	13.5	51300±7100	9260±670	16±2	28±3	282±15	132±10	57600±4200	17000±5000	523±34	153±13	233±46	14500	329±54
C3-6	20.0	46900±5800	9720±620	18±2	26±2	276±15	127±7	53000±3300	15700±4200	466±30	138±9	276±48	15000	325±50
C3-7	30.0	54100±15500	9840±1490	28±5	37±7	475±89	221±48	58200±11600	18200±4300	47886±	176±31	600±124	28000	531±123
C3-8	40.0	40900±5300	9330±540	68±5	103±6	511±24	170±8	49400±3100	15100±3500	364±18	177±10	739±102	15800	426±56
C3-9	55.0	39800±5400	10300±600	214±16	28±2	792±34	205±11	47500±2900	14400±3500	379±19	136±9	1371±220	16900	486±69
C3-10	75.0	31100±4100	10000±660	391±33	18±2	869±43	214±11	49100±2700	13900±3200	503±30	119±7	1005±137	14700	428±61
C3-11	95.0	41700±5100	10500±700	0.9±0.6	24±1	184±9	40±4	52200±2900	12600±2800	490±23	155±9	73±11	10900	125±17

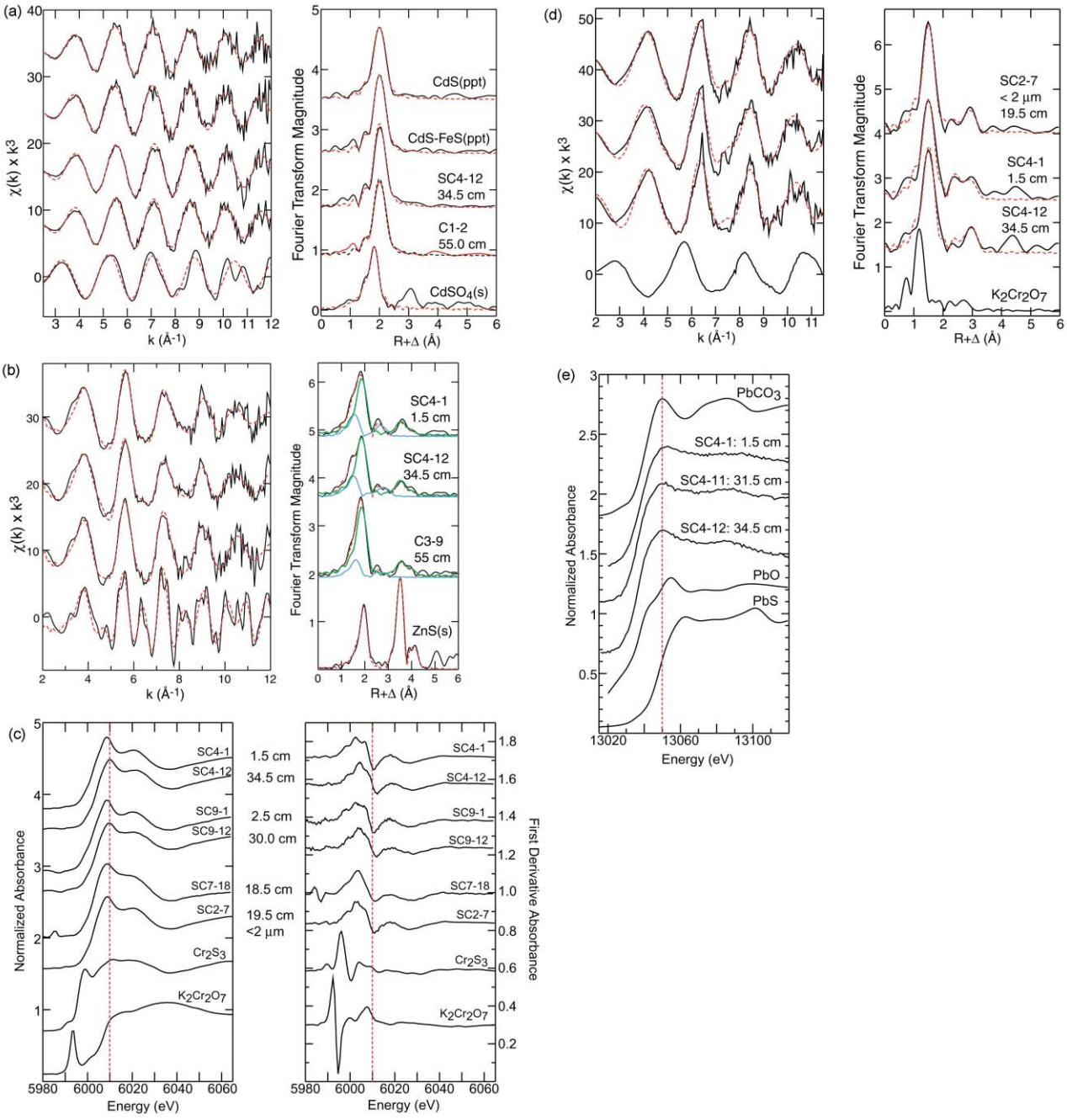

Fig. 4 (a) Normalized EXAFS and corresponding radial structure functions (uncorrected for phase shift of backscattering atoms) for cadmium in two NAS Alameda sediment samples from core SC4-12 (34.5 cm) and core C1-2 (5.5 cm) compared to reference precipitates, cadmium sulfide (CdS(ppc)) and a mixture of cadmium and iron sulfide (CdS–FeS) precipitated from solution immediately before data collection, and crystalline cadmium sulfate ($CdSO_4$(s)). Dashed red line is the non-linear least-squares best fit. (b) Normalized EXAFS and corresponding radial structure functions (uncorrected for phase shift of backscattering atoms) for zinc in sediment samples from core SC4 (at 1.5 and 34.5 cm) and core C3-9 (55 cm) compared to a reference spectrum of crystalline sphalerite (ZnS(s)). Dashed red line is the non-linear least-squares best fit; green line is the fit component corresponding to sphalerite; blue line is the fit for a zinc–oxygen component that probably represents zinc substitution in detrital phyllosilicate or oxide minerals. (c) Normalized XANES spectra and corresponding first-derivative spectra for chromium in samples from cores SC4 (at 1.5 and 34.5 cm), SC9 (at 2.5 and 30 cm) and SC7 (at 18.5 cm) compared with reference spectra for crystalline chromium sulfide and potassium chromate compounds. (d) Normalized EXAFS and corresponding radial structure functions (uncorrected for phase shift of backscattering atoms) for chromium in sediment samples SC2-7, SC4-1, and SC4-12 compared to reference crystalline potassium chromate. Dashed red line is the non-linear least-squares best fit. Oxidation of Cr(III) to Cr(VI) results in a significant shift of the first-shell oxygen peak to shorter interatomic distance. (e) Normalized XANES spectra for lead in samples from core SC4 (at 1.5, 31.5, and 34.5 cm) compared with reference spectra for crystalline lead sulfide, oxide, and carbonate compounds.

SC4. The oxide component comprises 22–25% of the zinc atomic component even though total zinc concentration increases from 287 μg g^{-1} at 2.5 cm to 515 μg g^{-1} at 34.5 cm. In a different core (C3), a sample from 55 cm depth shows a higher relative proportion of sulfide component, about 90%, although the total zinc concentration (486 μg g^{-1}) is similar to that of core SC4 at 34.5 cm (515 μg g^{-1}).

3.3.2 Oxide-associated metals. Both chromium and lead are associated with oxide phases in the sediments and there is no evidence for association with sulfide minerals. Analyses of XANES (Fig. 4c) and EXAFS (Fig. 4d) spectra for chromium show no evidence for the presence of sulfur backscatterers and indicate Cr(III) only. The presence of Cr(VI) would be readily apparent by a distinctive pre-edge feature in the XANES

Table 6 EXAFS analyses

Cadmium EXAFS analysis

Core	Atom	R/Å	N	σ^2/Å^2	ΔE_0/eV
Sediments					
SC4-12	Cd–S[a]	2.50[e]	4.0	0.0044[e]	−1.0[e]
34.5 cm					
192 ppm					
C1-2	Cd–S[a]	2.51[e]	4.0	0.0051[e]	−1.4[e]
55.0 cm					
1222 ppm					
SC4-11	Cd–S[b]	2.51	1.9[e]	0.0050	−4.1[e]
31.5 cm	Cd–O[b]	2.31[e]	3.2[e]	0.0120[e]	
Leached					
Reference precipitates[c]					
$Cd_{1.0}S$	Cd–S	2.51[e]	4.0	0.0056[e]	−1.7[e]
$Cd_{0.25}S$	Cd–S	2.51[e]	4.0	0.0048[e]	−2.6[e]
Reference compound: greenockite (CdS)[d]					
	Cd–S	2.52	1		
	Cd–S	2.53	3		
	Cd–Cd	4.12	6		
	Cd–Cd	4.13	6		

Scale factor (S_0^2) = 1.5. [a] First-shell Cd–S coordination fixed at 4; R and σ^2 were varied. [b] For the sulfide component, R and σ^2 were fixed on the average of values determined from fits to reference precipitates; N was varied. If $N_{Cd-S} = 4$ and $N_{Cd-O} = 6$ are assumed, then the sulfide component is 47% and the oxide component is 53% of the total absorption spectrum. [c] Cadmium sulfide was precipitated by adapting an FeS method.[10] XAS spectra collected on wet samples immediately after precipitation. [d] Crystallographic values for greenockite from ref. 58. [e] Parameter varied in least-squares fits.

Zinc EXAFS analysis

Core	Rel. %	Atom	R/Å	N	σ^2/Å^2	ΔE_0/eV
Sulfide component[f]						
SC4-1	75	Zn–S	2.33	3.0[l]	0.0065	−5.2[l]
2.5 cm		Zn–Zn	3.83	8.9	0.0231[l]	
287 ppm		Zn–S	4.49	8.9	0.0267[l]	
SC4-12	78	Zn–S	2.33	3.1[l]	0.0065	−6.3[l]
34.5 cm		Zn–Zn	3.83	9.3	0.0221[l]	
515 ppm		Zn–S	4.49	9.3	0.0297[l]	
C3-9	90	Zn–S	2.33	3.6[l]	0.0065	−5.2[l]
55.0 cm		Zn–Zn	3.83	10.8	0.0259[l]	
486 ppm		Zn–S	4.49	10.8	0.0257[l]	
SC4-11	25	Zn–S	2.33	0.9[l]	0.0065	−5.9[l]
31.5 cm		Zn–Zn	3.82	2.6	0.0225[l]	
Leached		Zn–S	4.49	2.6	0.0139[l]	
Oxide component[g]						
SC4-1	25	Zn–O	2.04[l]	1.7[l]	0.0065	−5.2[l]
2.5 cm		Zn–Me[h]	3.13[l]	1.0[l]	0.0080	
287 ppm		Zn–Me[i]	3.13[l]	0.8[l]	0.0100	
SC4-12	22	Zn–O	1.99[l]	1.4[l]	0.0065	−6.3[l]
34.5 cm		Zn–Me[h]	3.06[l]	0.9[l]	0.0080	
515 ppm		Zn–Me[i]	3.13[l]	0.8[l]	0.0080	
		Zn–Me[j]	3.21[l]	1.7[l]	0.0080	
C3-9	10	Zn–O	2.09[l]	1.4[l]	0.0065	−5.2[l]
55.0 cm		Zn–Me[f]	3.10[l]	0.4[l]	0.0080	
486 ppm						
SC4-11	75	Zn–O	2.02[l]	3.2[l]	0.0065	−5.9[l]
31.5 cm		Zn–Me[h]	3.13[l]	1.3[l]	0.0080	
Leached		Zn–Me[j]	3.39[l]	0.6[l]	0.0080	
Reference compound: sphalerite (ZnS)[k]						
		Zn–S	2.33	4		
		Zn–Zn	3.83	12		
		Zn–S	4.49	12		

Scale factor (S_0^2) = 1.0. [f] Sulfide component: Interatomic distances (R) for Zn–S and Zn–Zn fixed on crystallographic values in sphalerite; first-shell σ^2 for Zn–S was fixed on an empirical value determined from fits to sulfide reference compounds. For higher Zn–Zn and Zn–S shells, N was fixed on the value calculated from the proportion of sphalerite component determined in fits to filtered first-shell spectra and σ^2 was varied. [g] Oxide component: Values for σ^2 were fixed for all shells based on empirical fits to reference compounds; R and N were varied. [h] Backscatterer is Fe or similar transition metal cation; edge-sharing octahedra. [i] Backscatterer is Mg or Al; edge-sharing octahedra. [j] Backscatterer is Fe or Si; corner-sharing octahedra or tetrahedra. [k] Crystallographic values for sphalerite from ref. 28. [l] Parameter varied in least-squares fit.

Table 6 EXAFS analyses *(continued)*

Chromium EXAFS analysis

Core	Atom	R/Å	N	σ^2/Å^2	ΔE_0/eV
Oxide component[m]					
SC2-7	Cr–O	1.97[s]	6.0	0.0035[s]	−8.5[s]
19.5 cm	Cr–Me[n]	3.01[s]	1.9[s]	0.0100	
<2 μm	Cr–Me[o]	3.00[s]	1.7[s]	0.0100	
392 ppm	Cr–Fe	3.42[s]	1.8[s]	0.0080	
SC4-1	Cr–O	1.98[s]	6.0	0.0041[s]	−8.9[s]
1.5 cm	Cr–Me[p]	2.97[s]	1.6[s]	0.0080	
243 ppm	Cr–Fe	3.44[s]	1.9[s]	0.0080	
SC4-12	Cr–O	1.97[s]	6.0	0.0041[s]	−6.0[s]
34.5 cm	Cr–Me[p]	3.02[s]	1.1[s]	0.0100	
766 ppm	Cr–Fe	3.44[s]	2.2[s]	0.0080	
SC4-11	Cr–O	1.98[s]	6.0	0.0037[s]	−8.8[s]
31.5 cm	Cr–O[p]	3.00[s]	1.8[s]	0.0100	
Leached	Cr–Fe	3.42[s]	1.2[s]	0.0080	
Reference compounds					
Cr_2S_3[q]	Cr–S	2.42	6		
	Cr–Cr	2.79	2		
	Cr–S	4.20	6		
$K_2Cr_2O_7$[r]	Cr–O	1.52, 1.54, 1.73, 1.85	4		
	Cr–Cr	3.13	1		
	Cr–K	3.26	1		

Scale factor (S_0^2) = 0.90. [m] Oxide component: First-shell Cr–O coordination fixed at 6; σ^2 was varied. For higher shells, values for σ^2 were fixed based on empirical fits to reference compounds; R and N were varied. [n] Backscatterer is Mg or Al; edge-sharing octahedra. [o] Backscatterer is Fe or similar transition metal cation; edge-sharing octahedra. [p] Fit with single shell of Fe atoms; probably a disordered shell of Al, Mg, and Fe atoms. [q] Crystallographic values from ref. 59. [r] Crystallographic values from ref. 60. [s] Parameter varied in least-squares fits.

Iron EXAFS analysis

Core	Rel. %	Atom	R/Å	N[w]	σ^2/Å^2	ΔE_0/eV
Pyrite component[t]						
SC4-1	35.6	Fe–S	2.25	0.80	0.0011	−7.2[w]
2.5 cm		Fe–S	3.44	0.80	0.0066	
		Fe–Fe	3.82	1.60	0.0066	
SC4-12	38.5	Fe–S	2.25	0.92	0.0011	−6.7[w]
34.5 cm		Fe–S	3.44	0.92	0.0066	
		Fe–Fe	3.82	1.84	0.0066	
SC4-11	21.4	Fe–S	2.25	0.66	0.0011	−8.3[w]
31.5 cm		Fe–S	3.44	0.66	0.0066	
Leached		Fe–Fe	3.82	1.32	0.0066	
Oxide component[u]						
SC4-1	64.4	Fe–O	2.00[w]	2.64	0.0048	−3.4[w]
2.5 cm		Fe–Fe	3.10[w]	0.53	0.0050	
		Fe–Si	3.26	1.43	0.0057	
		Fe–Fe	3.39[w]	0.29	0.0057	
SC4-12	61.5	Fe–O	2.00[w]	2.79	0.0048	−3.2[w]
34.5 cm		Fe–Fe	3.09[w]	0.62	0.0050	
		Fe–Si	3.26	1.15	0.0057	
		Fe–Fe	3.43[w]	0.41	0.0057	
SC4-11	78.6	Fe–O	2.00[w]	3.12	0.0048	−0.5[w]
31.5 cm		Fe–Fe	3.09[w]	0.92	0.0050	
Leached		Fe–Si	3.26	0.82	0.0057	
		Fe–Fe	3.39[w]	0.41	0.0057	

Table 6 EXAFS analyses *(continued)*

Reference compound: pyrite (FeS_2)[v]		
Fe–S	2.25	6
Fe–S	3.44	6
Fe–Fe	3.82	12

[t] Pyrite component: Interatomic distances (R) were fixed on crystallographic values from pyrite and σ^2 was fixed on values determined from fits to reference sulfide compounds. N for each shell was floated as a linked variable in proportions based on the known coordination in pyrite. Relative percent (Rel. %) for pyrite or oxide components is calculated from the integrated fit areas of all atomic shells comprising each component (normalized to 100%). [u] Oxide component: Values for σ^2 were fixed for all shells based on empirical fits to reference compounds of similar composition and structure; R and N were varied, except for the Fe–Si shell, which will co-vary with Fe shells if floated independently. This shell was fixed on a typical crystallographic distance for Fe–Si in phyllosilicates. [v] Crystallographic values from ref. 61. [w] Parameter varied in least-squares fit.

spectrum and by much shorter Cr–O distances than obtained in first coordination shell fits to the EXAFS spectra (Table 6). Comparison of normalized and first-derivative XANES spectra for shallow and deep sediments from two cores (SC4 and SC9) are very similar, with slight differences in spectral shape above the energy of maximum absorption revealed in first-derivative spectra (Fig. 4c). XANES spectra of two samples from intermediate depths (SC7-18 and SC2-7) are very similar to the chromium spectra of shallow cores.

Likewise, EXAFS spectra for three sediment samples are generally very similar regardless of total chromium concentration which increases with depth in core SC4 from 245 μg g^{-1} at 1.5 cm to 766 μg g^{-1} at 34.5 cm. All spectra have identical first-shell coordination and slight differences in backscattering amplitudes for more distant atomic shells (Fig. 4d and Table 6). Interatomic distances obtained from EXAFS fits do not correspond to a single identifiable chromium oxide phase. First coordination shell Cr–O distances are typical of octahedral coordination of Cr(III) by oxygen in oxide and silicate compounds. Distances obtained from fitting of higher shells are consistent with edge-sharing of metal octahedra and corner-sharing of metal octahedra and/or tetrahedra. Differences in the amplitude of backscattering from atoms at 2.97–3.02 Å appear to be related to cancellation effects among atoms such as iron (or similar Z elements), magnesium, and aluminium at slightly different Cr–Me interatomic distances. Backscattering from atoms at 3.42–3.44 Å is more consistent and best fit with iron. These structural results are consistent with chromium substitution in phyllosilicates, association with spinel phases such as chromite or magnetite, and/or inner-sphere adsorption on oxides or silicates. As discussed below, chromium in the sediments originates from both contaminant and detrital sources, with the contaminant fraction dominant in deeper sediments. The spectral results, however, do not indicate major changes in chromium bonding with depth.

Comparison of XANES spectra for lead in the sediments and in reference compounds indicates that lead is bonded by oxygen. Coordination of lead by sulfur would result in a shift of maximum absorption at the Pb L_{III} edge to significantly lower energy (Fig. 4e). The energy of maximum absorption is consistent with lead coordination in either oxide, phosphate, or carbonate phases. There are no changes in the XANES spectra of samples from core SC4 even though the total lead concentration increases significantly from 214 μg g^{-1} at 1.5 cm to 1269 μg g^{-1} at 34.5 cm. Previous analysis of first-neighbor atomic scattering in one lead EXAFS spectrum (SC9-12, 30 cm depth) indicated the presence of oxygen atoms only.[22] Quantitative analyses of two lead EXAFS spectra from core SC4 were precluded by poor data quality, but there was no evidence for backscattering from sulfur atoms. Lead exhibits high static disorder in its local oxygen coordination in a

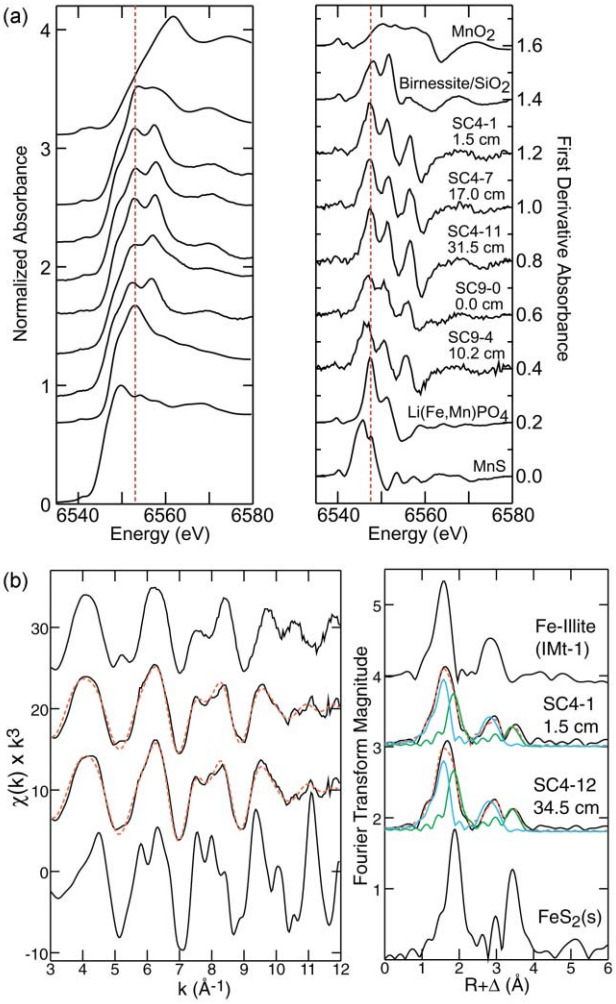

Fig. 5 (a) Normalized XANES spectra and corresponding first-derivative spectra for manganese in samples from cores SC4 (at 1.5, 17.0, and 31.5 cm) and SC9 (at 0.0 and 10.2 cm) compared with reference spectra for synthetic manganese(IV) oxide (MnO_2, pyrolusite), birnessite (layered Mn(III,IV) oxide) precipitated on quartz (birnessite/SiO_2), a natural Mn-phosphate (Li(Fe, Mn)PO_4, ferrisicklerite), and Mn(II) sulfide (MnS). (b) Normalized EXAFS and corresponding radial structure functions (uncorrected for phase shift of backscattering atoms) for iron in sediment samples from core SC4 (at 1.4 and 34.5 cm) compared to reference spectra of crystalline pyrite (FeS_2(s)) and of iron substituted in reference illite IMt-1 (Clay Minerals Source Repository). Dashed red line is the non-linear least-squares best fit; green line is the fit component corresponding to pyrite; blue line is the fit for an iron–oxygen component that probably represents iron substitution in phyllosilicate or oxide minerals.

number of lead oxide, (oxy)hydroxide, phosphate, and carbonate compounds, and thus, first coordination shell distances are not diagnostic of a particular phase.[16,23,24] Evidence from the XANES and EXAFS spectra are consistent with lead coordination in either carbonate, phosphate, or (oxy)hydroxide phases, or as an oxygen-ligated sorbed complex.

3.3.3 Manganese and iron. Manganese concentrations in the sediments vary between 350–550 μg g^{-1} and do not generally increase with depth, as do the contaminant metals. Comparison of the manganese XANES spectra as a function of depth in core SC4 indicates no significant changes among samples between 1.5 and 31.5 cm (Fig. 5a). Examination of first-derivative XANES spectra shows only slight variations in the energy positions of major inflection points among the sediment samples. The sediment XANES spectra could not be entirely fit with a single reference compound or by linear combinations of two or three manganese reference compounds, including combinations of carbonate, phosphate, sulfate, sulfide, and

oxide minerals. This suggests that manganese is substituting in other minerals or forming solid solutions rather than forming pure manganese compounds. Absorption edge features from ~6548–6555 eV are similar to a natural speciman of ferrisicklerite ($Li[Fe^{3+},Mn^{2+}]PO_4$), a mixed iron–manganese phosphate mineral, indicating a phosphate component that comprises roughly one-third to one-half of the manganese in the sediment samples. Two samples from a different core, SC9 collected in April 1998, show some spectral features below ~6548 eV that can be attributed to manganese associated with sulfide, which is variable among samples and comprises from 0 to ~20% of manganese in the sediments.† Absorption features above 6555 eV could not be well fit with pure manganese reference compounds. The sediment samples have a second absorption maximum at 6557–6558 eV, which is near to observed maxima for Mn(III) and Mn(II,III) oxide compounds.[25,26] Manganese(IV) oxide compounds generally have absorption maxima at higher energy (6560 eV or above) (Fig. 5a). These comparisons suggest that a large fraction of manganese is bonded predominately in an oxide component as Mn(III) or as a mixture of Mn(II,III). This is consistent with substitution of manganese into detrital phyllosilicate or oxide minerals in concentrations on the order of 100–300 μg g^{-1} (about half of the total manganese sediment concentrations).

Iron in the sediments is a major element, occurring in concentrations of about 4–6 wt% (Fig. 3 and Table 5). Analyses of EXAFS spectra from core SC4 indicate both sulfide and oxide iron components (Fig. 5b). The sulfide component is clearly identified as pyrite based on interatomic distances derived from fits of Fe–S and Fe–Fe shells (Table 6). In the sediment samples, backscattering amplitudes are lower for Fe–S and Fe–Fe shells beyond the first sulfur coordination shell than in the crystalline pyrite reference compound (Fig. 5b). This suggests poor crystallinity and/or small particle size.[27] Iron monosulfide (amorphous FeS or crystalline mackinawite), which has a different atomic structure than pyrite,[28] could not be fit in the spectra. If FeS is present, it must comprise less than about 5 atom% of total iron to be undetected in the EXAFS spectra.[22] Analyses of XANES spectra indicates that below ~1–2 cm depth the primary iron oxide component in the sediment is a phyllosilicate which is most similar in structure to iron substituted into mica (*e.g.*, illite, muscovite, or biotite).[29] Other minor iron oxide components that might be present include chlorite and magnetite. Based on qualitative information from XANES spectra, the oxide component in the EXAFS spectra was fit with four shells (Table 6), Fe–O at 2.00 Å, Fe–Fe at 3.08–3.10 Å, Fe–Si at 3.26 Å, and Fe–Fe at 3.39–3.42 Å, to account for all primary Fe–X distances in phyllosilicates and Fe(III) oxides (if present). Based on EXAFS fits to core SC4 spectra, the relative proportion of iron in pyrite compared to oxide phases increases only slightly with depth (~3%) from 1.5 to 34.5 cm with no change in interatomic distances. Over this interval, total iron concentration increases from 4.4 to 5.3 wt%.

3.4 Reaction rates from oxidation experiments

Trace metal dissolution during the sediment oxidation experiments are shown in Fig. 6 as the net rate and the percent metal dissolved *versus* time. The rates of reaction for each element were calculated according to:

$$\text{Rate (day}^{-1}) = \Delta[i]_{aq} \times FR \times (wt_{sediment} \times [i]_{sediment})^{-1}$$

where $\Delta[i]_{aq}$ (10^{-6} g g^{-1}) is the difference in concentration between the output and input (seawater blank) solutions, FR

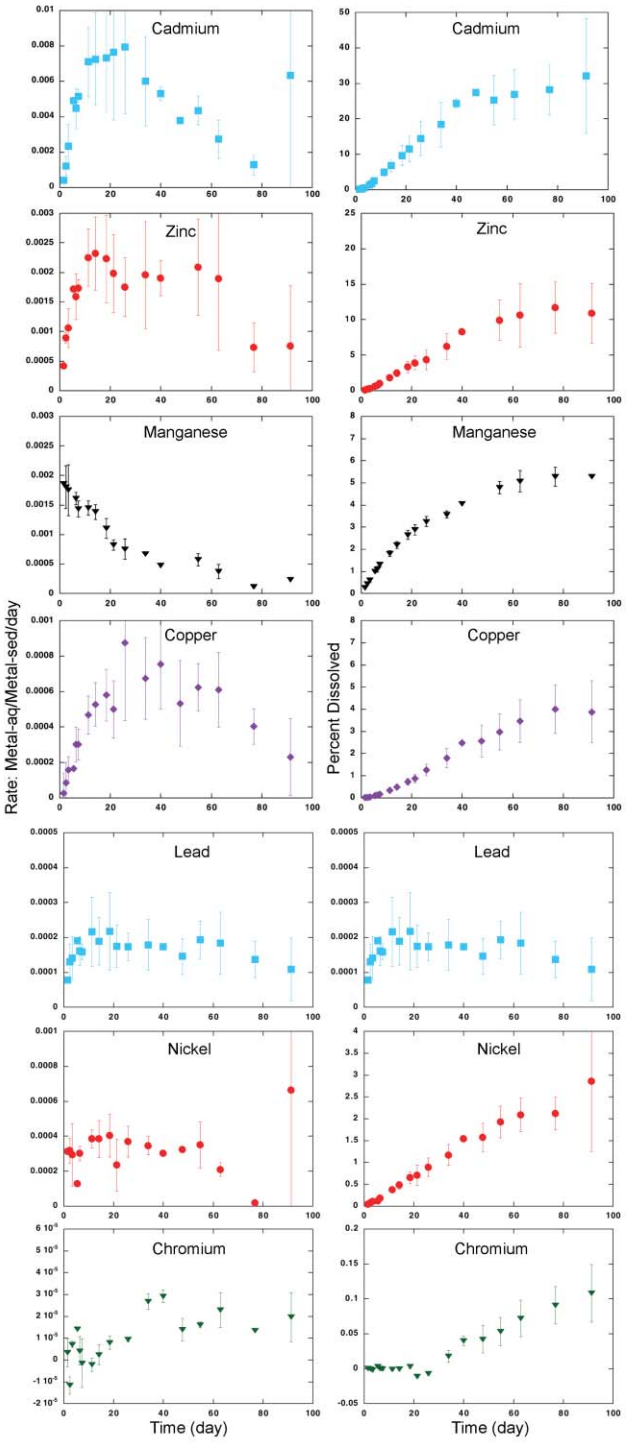

Fig. 6 Oxidation rates of reduced sediments (SC4-11) in seawater plotted as the metal concentration dissolved per day normalized to the remaining metal concentration in the sediment (right side) and as the total metal concentration dissolved normalized to the initial metal concentration in the sediment (left side).

(g day^{-1}) is the flow rate, and ($wt_{sediment}$ (g) × $[i]_{sediment}$ (10^{-6} g g^{-1})) is the total concentration of each element in the sediment. We use the respective seawater blank analyses as our input solutions to directly correct for any trace metal contamination from the laboratory environment as a function of time (the experiments were not conducted in a Class 100 clean room). Normalization to total concentration allows reactivity among the metals to be compared directly. We also show the total metal dissolved as the percent metal dissolved normalized to the concentration of the initial metal in the sediment *versus* time. The averaged rates, percent metal dissolved, and associated uncertainties are calculated from the triplicate experiments (Table 7).

† Based on the analysis of one EXAFS spectrum, the Mn sulfide component was previously overestimated in O'Day *et al.*[22] Re-analyses of XANES spectra suggest at most about 20% Mn sulfide in the sediments.

Table 7 Results of leaching experiments with sediment SC4-11 (runs A, B, C, and blank) as dissolved trace-metal concentrations[a]

Sediment SC4-11-A

Sample ID	Time/ days	Flow rate/g day^{-1}	pH	Cd (ppb)	Cr (ppb)	Cu (ppb)	Mn (ppb)	Ni (ppb)	Pb (ppb)	Zn (ppb)
SC4-11-A-1	0.47	a	8.01	0.78±0.02	0.75±0.51	3.82±0.11	42.5±1.6	2.98±0.08	1.26±0.01	16.45±0.37
SC4-11-A-2	1.42	41.92	7.78	2.12±0.03	0.44±0.24	1.29±0.10	22.0±0.7	2.20±0.03	1.92±0.02	11.39±0.10
SC4-11-A-3	2.35	42.65	7.81	3.95±0.05	0.24±0.13	1.34±0.04	17.5±0.4	1.79±0.03	2.67±0.03	16.59±0.29
SC4-11-A-4	3.34	42.97	7.82	6.50±0.09	0.31±0.11	1.47±0.05	16.1±0.4	1.42±0.04	2.98±0.01	17.55±0.23
SC4-11-A-5	4.41	43.47	7.87	na	na	na	na	na	na	na
SC4-11-A-6	5.42	43.58	7.87	na	na	na	na	na	na	na
SC4-11-A-7	6.39	43.91	7.83	11.20±0.14	0.22±0.11	1.85±0.13	18.7±0.8	1.55±0.03	2.84±0.01	17.16±0.37
SC4-11-A-8	7.37	43.75	7.81	na	na	na	na	na	na	na
SC4-11-A-9	11.36	44.64	7.93	16.14±0.25	0.32±0.05	2.66±0.10	17.7±0.4	2.18±0.04	2.82±0.03	23.43±0.16
SC4-11-A-10	14.19	45.04	7.82	13.74±0.11	0.28±0.04	2.68±0.12	14.7±0.5	1.90±0.02	2.65±0.01	22.48±0.43
SC4-11-A-11	18.43	45.31	7.82	12.77±0.16	0.31±0.06	2.64±0.07	12.9±0.5	1.92±0.04	2.51±0.03	18.88±0.14
SC4-11-A-12	21.23	45.53	7.86	11.54±0.04	0.26±0.10	2.34±0.07	10.9±0.4	1.80±0.03	2.50±0.01	17.41±0.24
SC4-11-A-13	25.72	46.56	7.77	10.92±0.13	0.39±0.28	3.31±0.04	10.5±0.4	2.03±0.02	3.01±0.01	18.63±0.24
SC4-11-A-14	33.86	46.91	7.82	9.45±0.11	0.41±0.05	2.43±0.08	8.50±1.40	2.00±0.04	2.32±0.05	12.82±0.20
SC4-11-A-15	39.91	47.81	7.87	na	na	na	na	na	na	na
SC4-11-A-16	47.75	41.16	8.05	na	0.38±0.09	1.99±0.08	na	2.21±0.30	2.30±0.28	na
SC4-11-A-17	54.75	44.60	7.81	10.11±0.23	0.44±0.11	2.90±0.09	8.00±0.30	2.10±0.07	3.13±0.01	18.08±0.41
SC4-11-A-18	62.91	44.80	7.85	6.93±0.14	0.41±0.15	2.39±0.06	5.90±0.90	1.76±0.01	2.21±0.06	11.91±0.22
SC4-11-A-19	76.90	48.08	7.87	2.81±0.04	0.41±0.13	1.77±0.04	2.70±0.20	1.16±0.03	1.88±0.02	7.58±0.08
SC4-11-A-20	91.41	47.53	7.94	1.34±0.10	0.36±0.21	1.00±0.01	na	0.88±0.02	1.02±0.05	3.91±0.36

Sediment SC4-11-B

Sample ID	Time/ days	Flow rate/g day^{-1}	pH	Cd (ppb)	Cr (ppb)	Cu (ppb)	Mn (ppb)	Ni (ppb)	Pb (ppb)	Zn (ppb)
SC4-11-B-1	0.47	a	7.98	0.42±0.02	nd	0.91±0.04	36.9±0.7	1.26±0.04	1.83±0.05	6.88±0.25
SC4-11-B-2	1.42	41.52	7.85	na	na	na	na	na	na	na
SC4-11-B-3	2.35	42.12	7.82	4.89±0.05	nd	1.06±0.06	18.6±0.5	1.86±0.05	3.51±0.03	13.66±0.16
SC4-11-B-4	3.34	42.59	7.86	9.71±0.11	0.32±0.113	1.41±0.09	19.1±0.7	2.21±0.04	3.87±0.04	17.59±0.26
SC4-11-B-5	4.41	43.10	7.86	na	na	na	na	na	na	na
SC4-11-B-6	5.42	a	7.86	na	na	na	na	na	na	na
SC4-11-B-7	6.39	43.73	7.86	11.59±0.13	0.37±0.114	2.07±0.06	15.4±0.6	1.45±0.05	3.03±0.02	19.62±0.33
SC4-11-B-8	7.37	43.84	7.84	12.12±0.42	0.28±0.074	1.85±0.12	13.8±0.4	nd	2.54±0.08	19.94±1.06
SC4-11-B-9	11.36	44.77	7.93	18.20±0.18	0.36±0.053	2.57±0.12	13.7±0.3	2.04±0.03	3.69±0.04	23.71±0.28
SC4-11-B-10	14.19	45.36	7.79	19.87±0.15	0.37±0.045	2.85±0.12	12.7±0.3	2.12±0.07	3.72±0.05	24.53±0.16
SC4-11-B-11	18.43	46.43	7.80	21.20±0.24	0.33±0.057	3.01±0.07	11.2±0.2	2.25±0.04	3.61±0.04	24.59±0.17
SC4-11-B-12	21.23	46.81	7.80	23.01±0.09	0.45±0.096	2.96±0.11	9.16±0.16	2.22±0.04	3.38±0.04	22.65±0.18
SC4-11-B-13	25.72	47.68	7.80	18.43±0.29	0.33±0.276	2.66±0.11	6.17±0.37	2.17±0.06	2.99±0.06	19.27±0.32
SC4-11-B-14	33.86	48.92	7.81	14.20±1.41	0.38±0.050	2.66±0.10	na	1.85±0.04	3.09±0.29	22.52±3.77
SC4-11-B-15	39.91	50.83	7.86	8.27±0.09	0.37±0.045	3.31±0.07	3.73±0.22	1.61±0.01	2.62±0.07	15.25±0.25
SC4-11-B-16	47.75	41.34	7.86	7.42±1.28	0.42±0.087	2.35±0.06	na	1.84±0.13	3.11±0.35	na
SC4-11-B-17	54.75	44.49	7.79	7.74±0.28	0.40±0.112	2.61±0.11	4.60±0.54	1.70±0.05	3.68±0.10	19.64±1.02
SC4-11-B-18	62.91	44.76	7.80	6.70±0.74	0.44±0.148	2.49±0.08	na	1.46±0.05	3.36±0.23	15.42±2.17
SC4-11-B-19	76.90	42.20	7.87	3.49±0.06	0.38±0.134	2.08±0.06	2.28±0.14	1.10±0.04	2.57±0.06	8.68±0.12
SC4-11-B-20	91.41	49.85	7.87	15.24±0.29	0.46±0.214	1.84±0.03	2.83±0.42	4.16±0.05	2.62±0.21	13.79±0.36

Sediment SC4-11-C

Sample ID	Time/ days	Flow rate/g day^{-1}	pH	Cd (ppb)	Cr (ppb)	Cu (ppb)	Mn (ppb)	Ni (ppb)	Pb (ppb)	Zn (ppb)
SC4-11-C-1	0.47	a	7.96	0.52±0.01	1.00±0.51	13.71±0.26	43.2±1.3	4.96±0.12	2.13±0.02	22.43±0.31
SC4-11-C-2	1.42	41.64	7.66	1.15±0.01	0.30±0.24	2.09±0.10	22.0±0.5	1.97±0.06	1.96±0.00	10.96±0.15
SC4-11-C-3	2.35	42.49	7.84	2.50±0.00	0.34±0.13	2.07±0.06	21.2±0.5	1.65±0.03	2.21±0.02	13.31±0.13
SC4-11-C-4	3.34	43.00	7.85	4.55±0.02	0.32±0.11	2.02±0.07	19.8±0.4	1.49±0.05	2.06±0.01	12.71±0.13
SC4-11-C-5	4.41	43.67	7.85	na	na	na	na	na	na	na
SC4-11-C-6	5.42	43.84	7.86	14.59±0.20	0.45±0.07	1.38±0.07	17.3±0.6	1.17±0.03	3.97±0.03	21.49±0.16
SC4-11-C-7	6.39	44.19	7.84	16.04±0.06	0.29±0.11	1.54±0.05	16.1±0.3	1.67±0.06	4.09±0.04	21.71±0.13
SC4-11-C-8	7.37	44.33	7.86	15.70±0.07	0.27±0.07	1.54±0.08	14.1±0.4	na	3.63±0.04	20.65±0.23
SC4-11-C-9	11.36	45.42	7.91	23.54±0.11	0.28±0.05	2.05±0.12	13.6±0.3	2.30±0.03	6.34±0.05	29.54±0.33
SC4-11-C-10	14.19	46.02	7.83	22.85±0.24	0.39±0.04	2.43±0.15	14.4±1.0	2.33±0.08	4.73±0.06	31.06±0.37
SC4-11-C-11	18.43	47.27	7.80	19.52±0.17	0.29±0.06	2.80±0.19	9.88±0.21	2.21±0.02	6.30±0.07	28.26±0.36
SC4-11-C-12	21.23	47.04	7.74	19.52±0.10	0.26±0.10	2.97±0.06	8.88±0.12	na	4.18±0.03	25.56±0.09
SC4-11-C-13	25.72	48.10	7.81	23.94±3.95	nd±0.28	5.95±0.22	na	2.07±0.11	3.94±0.41	na
SC4-11-C-14	33.86	50.50	7.86	13.77±0.26	0.41±0.05	3.73±0.14	5.15±0.18	2.08±0.03	4.41±0.04	21.81±0.11
SC4-11-C-15	39.91	54.43	7.85	10.33±1.13	0.43±0.04	2.37±0.06	na	na	2.97±0.23	13.58±2.22
SC4-11-C-16	47.75	39.49	7.89	na	0.51±0.09	4.10±0.19	na	na	4.26±0.54	na
SC4-11-C-17	54.75	45.85	7.87	10.53±0.21	0.40±0.11	3.54±0.11	5.41±0.97	2.57±0.09	4.59±0.15	29.81±0.57
SC4-11-C-18	62.91	46.58	7.83	3.61±0.07	0.57±0.15	3.69±0.10	3.62±0.11	1.76±0.04	5.19±0.04	24.20±0.26
SC4-11-C-19	76.90	51.01	7.88	1.59±0.28	0.38±0.13	2.17±0.05	na	1.13±0.10	3.37±0.40	12.89±3.12

Table 7 Results of leaching experiments with sediment SC4-11 (runs A, B, C, and blank) as dissolved trace-metal concentrations[a] *(continued)*

Blank

Sample ID	Time/ days	Flow rate/g day^{-1}	pH	Cd (ppb)	Cr (ppb)	Cu (ppb)	Mn (ppb)	Ni (ppb)	Pb (ppb)	Zn (ppb)
B-1	0.47	a	8.01	0.621±0.020	0.37±0.51	2.56±0.05	2.77±0.51	3.70±0.21	0.301±0.010	20.1±1.2
B-2	1.42	40.14	8.04	0.202±0.003	0.32±0.24	1.58±	1.98±0.24	0.88±0.02	0.124±0.002	6.07±0.15
B-3	2.35	41.16	8.02	0.185±0.003	0.46±0.13	1.09±0.05	1.75±0.13	0.67±0.02	0.089±0.002	4.51±0.06
B-4	3.34	41.55	8	0.120±0.002	0.22±0.11	0.92±0.05	1.77±0.1	0.75±0.02	0.077±0.002	4.43±0.10
B-5	4.41	42.10	8.02	0.141±0.003	0.29±0.17	0.86±0.02	1.87±0.173	0.68±0.03	0.075±0.002	3.78±0.06
B-6	5.42	a	7.97	0.127±0.005	0.27±0.07	0.65±0.04	1.77±0.07	0.73±0.04	0.047±0.001	2.86±0.07
B-7	6.39	42.87	7.96	0.103±0.004	nd	0.52±0.03	1.61±0.11	0.55±0.03	0.041±0.001	2.74±0.04
B-8	7.37	42.96	8.1	0.124±0.004	0.22±0.07	0.50±0.03	1.73±0.08	0.68±0.02	0.062±0.001	3.28±0.04
B-9	11.36	44.27	7.96	0.103±0.005	0.35±0.05	0.44±0.04	1.72±0.05	0.91±0.03	0.041±0.001	2.45±0.04
B-10	14.19	44.61	8	0.126±0.002	0.32±0.05	0.46±0.03	1.54±0.05	0.89±0.03	0.039±0.001	2.75±0.02
B-11	18.43	45.35	7.94	0.110±0.002	0.22±0.06	0.47±0.02	1.69±0.06	0.88±0.02	0.032±0.001	2.43±0.03
B-12	21.23	45.53	8	0.205±0.007	0.94±0.10	0.76±0.04	2.50±0.10	1.31±0.03	0.043±0.001	3.00±0.04
B-13	25.72	46.33	7.9	0.097±0.014	nd	0.46±0.02	1.68±0.28	0.96±0.08	nd	1.24±0.39
B-14	33.86	47.11	7.92	na	0.10±0.05	0.37±0.03	0.70±0.05	0.94±0.15	nd	2.07±0.37
B-15	39.91	49.35	7.92	na	0.11±0.05	0.37±0.03	0.60±0.05	na	nd	na
B-16	47.75	39.18	7.87	0.107±0.017	nd±0.09	0.37±0.02	1.22±0.09	na	na±0.000	na
B-17	54.75	41.97	7.89	0.107±0.017	0.21±0.11	0.43±0.03	0.84±0.11	0.98±0.11	0.027±0.002	1.52±0.45
B-18	62.91	43.29	8.06	0.097±0.014	0.20±0.15	0.39±0.02	1.20±0.15	0.98±0.09	nd	na
B-19	76.90	46.33	8	0.113±0.016	0.23±0.13	0.44±0.03	1.47±0.13	1.07±0.06	nd	3.47±0.65
B-20	91.41	49.13	7.92	0.087±0.002	0.20±0.21	0.64±0.02	1.26±0.21	0.92±0.01	0.013±0.000	3.53±0.11

[a] Flow rate not recorded, nd = not detected, na = not analyzed.

The net release of trace elements from the sediments is complex and metal specific. The cadmium, zinc, manganese, and copper release rates exhibit a rapid increase in dissolution rate during the initial oxidation (1 to 20 days), followed by continual decrease in release rates with time. After about 50 days of reaction, cadmium, zinc, manganese, and copper dissolution slows to about 30, 10, 5, and 4% of their respective initial sediment concentrations. After 90 days of reaction, the cadmium, zinc, manganese, and copper concentrations in the output solutions are near their respective concentrations in the top core section (1.5 cm, Table 2). The observed non-steady state dissolution behavior is indicative of concurrent dissolution of a reduced solid phase and precipitation of a stable secondary phase that limits the transfer of the trace metals to oxygen-rich seawater.

The net release rates of nickel, lead, and chromium are 10 to 100 times lower than the release rates of cadmium, zinc, manganese, and copper. Additionally the rates are more or less constant as a function of time, and show steady-state reaction kinetics. Nickel release rates are constant within the scatter of the data with the exception of one outlying data point at about 80 days. Lead release rates increase slightly during the first 10 days, are constant for the next 50 to 60 days, and decrease slightly after 80 days. Chromium release is characterized by minimal dissolution during the first 25 days followed by slightly greater dissolution rates that are constant for the duration of the experiment. These metals dissolve slowly with time; about 3% of the initial nickel, 1% of the initial lead and 0.1% of the initial chromium dissolve after the reduced sediments have reacted with seawater for 90 days.

For aluminium, calcium, potassium, iron, magnesium, and silica we observed minimal reactivity. There were no changes in the calcium, potassium and magnesium input and output concentrations. The dissolved iron, aluminium, and silica concentrations in the output solutions are below the analytical detection limits. This is expected because quartz, phyllosilicates, and iron oxides have very low dissolution rates in near-neutral seawater.

3.5 XAS analysis of metals in oxidized sediments

At the end of the 90 day oxidation experiment (SC4-11, 31.5 cm), sediments were re-examined with XAS to evaluate changes in oxidation state and local coordination compared to unreacted core sediments from similar depth. Cadmium, which was entirely coordinated by sulfur in unreacted sediments, is partially coordinated by oxygen in the reacted sample (Fig. 7a). Analyses of the EXAFS spectrum showed about 47% atomic coordination by oxygen and 53% coodination by sulfur. The interatomic Cd–S distances are identical to those of cadmium in unreacted sediments, indicating that the original CdS phase has not completely dissolved (Table 6). The Cd–O distance in the oxide component derived from EXAFS analysis (2.31 Å) is typical of cadmium oxide phases and oxygen-coordinated sorption complexes.[16,30,31] However, the lack of backscattering atoms beyond the first coordination shell suggests that the Cd–O component is not a well crystallized solid.

The X-ray absorption spectrum for zinc of the reacted sample likewise shows conversion of the original sulfide phase to an oxide phase (Fig. 7b). In unreacted sample SC4-12, 78% of zinc was coordinated by sulfur with local structure indicative of poorly crystalline sphalerite (ZnS). In reacted sample SC4-11, 25% of zinc remains coordinated in ZnS (distances are identical to unreacted samples) and 75% of zinc is coordinated by oxygen. As discussed previously, the original zinc oxide component may be a composite of zinc substituted into detrital silicate and oxide phases. These phases are probably recalcitrant during reaction with seawater and would not dissolve significantly. The absorption spectrum of the reacted sample is therefore a composite of residual ZnS, the original oxide component(s), and a new zinc oxide component. Least-squares fits of the EXAFS spectrum of the reacted sample indicate a first shell of oxygen atoms at an average distance of 2.03 Å and metal backscatterers at 3.13 Å, similar to unreacted samples (Table 6). There is also evidence for metal backscatterers at a longer distance (3.39 Å) which is indicative of corner sharing of metal octahedra or tetrahedra in (oxy)hydroxides and phyllosilicates. Owing to the complicated signal, backscattering in the oxide component could not be fit with unique elements beyond the coordinating shell of oxygen atoms. The interatomic distances obtained from fits, however, are consistent with zinc association with iron (oxy)hydroxide or phyllosilicate phases in addition to the original zinc oxide components (Fig. 7b).

In contrast to sulfide-associated metals, the XAS spectra

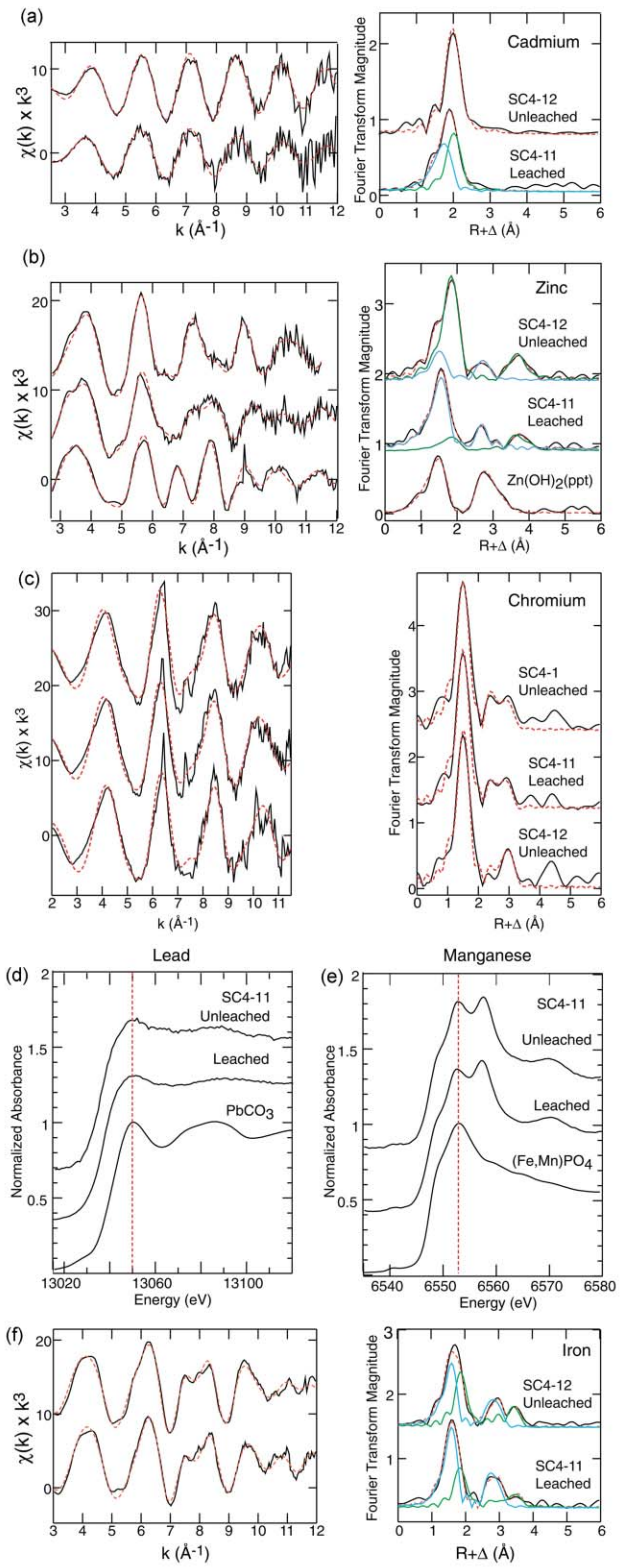

Fig. 7 (a) Normalized EXAFS and corresponding radial structure functions (uncorrected for phase shift of backscattering atoms) for cadmium in unleached and leached sediment samples from core SC4 at approximately the same depth (34 cm). Dashed red line is the non-linear least-squares best fit; green line is the fit component corresponding to CdS; blue line is the fit for a cadmium–oxygen component that probably represents cadmium adsorption on iron (oxy)hydroxides that form from pyrite oxidation. (b) Normalized EXAFS and corresponding radial structure functions (uncorrected for phase shift of backscattering atoms) for zinc in unleached and leached sediment samples from core SC4. Dashed red line is the non-linear least-squares best fit; green line is the fit component corresponding to sphalerite; blue line is the fit for a zinc–oxygen component that probably represents zinc adsorption on iron (oxy)hydroxides that form from pyrite oxidation and zinc substitution in phyllosilicate or oxide minerals noted previously. (c) Normalized EXAFS and corresponding radial structure functions (uncorrected for phase shift of backscattering atoms) for chromium in unleached and leached sediment samples from core SC4. Dashed red line is the non-linear least-squares best fit. (d) Normalized XANES spectra for lead in samples in unleached and leached sediment from core SC4 compared to reference crystalline lead carbonate ($PbCO_3$). (e) Normalized XANES spectra for manganese in samples in unleached and leached sediment from core SC4 compared to a reference manganese phosphate (Fe, $Mn(PO_4)$). (f) Normalized EXAFS and corresponding radial structure functions (uncorrected for phase shift of backscattering atoms) for iron in unleached and leached sediment samples from core SC4. Dashed red line is the non-linear least-squares best fit; green line is the fit component corresponding to pyrite; blue line is the fit for an iron–oxygen component that probably represents formation of an iron (oxy)hydroxide in addition to iron substitution in phyllosilicate or oxide minerals discussed previously.

of metals primarily associated with oxide phases show little change after reaction with seawater. There is no evidence in the chromium XAS data (XANES or EXAFS spectrum) for oxidation to Cr(VI), although a small percentage (<5 atom%) of surface-oxidized chromium cannot be ruled out based on the bulk spectrum. The EXAFS spectrum of the reacted sample most closely resembles that of the shallow sediment sample SC4-1 (1.5 cm) and differs slightly from that of sample SC4-12 (34.5 cm) (Fig. 7c). Fits indicate that these differences are related to the number of metal backscatterers beyond the first coordination shell of oxygen atoms and not to large changes in interatomic distances (Table 6). For lead and manganese, comparison of XANES spectra also indicates no signficant changes in local atomic coordination after reaction (Fig. 7d, e).

In the leached sediment sample, analysis of the iron EXAFS spectrum indicates a reduction of 17% in the fraction of the pyrite component compared to unreacted sediment SC4-12 (34.5 cm) based on integrated curve areas for fit pyrite and oxide components (Fig. 7f, Table 6). It is likely that iron lost from pyrite was resorbed or reprecipitated, probably as iron (oxy)hydroxides, because at most 1% of the iron was lost to solution (dissolved iron concentrations were below the detection limit of 100 ng g^{-1}). Analyses of the XANES spectrum of the leached sample indicates an small increase in the amount of Fe(III). Interatomic distances of the oxide component do not show any significant changes between reacted and unreacted sediments because distances among second-neighbor backscattering atoms in phyllosilicates and iron (oxy)hydroxides overlap (in the range of 3.03–3.15 Å). Backscattering amplitudes for second-neighbor atoms at 3.09–3.10 Å are higher in the leached sample compared to unleached samples, perhaps indicative of the precipitation of (oxy)hydroxides. At the pH of the leaching experiment (pH = 7.9), we expect minimal dissolution of phyllosilicates and quartz, precluding sources of aluminium and silica. The mostly likely phase for iron reprecipitation is amorphous iron (oxy)hydroxides.

4. Discussion

4.1 Trace metal geochemistry in estuarine sediments

The sediment cores represent a 60 year record of metal contamination in the Seaplane Lagoon as determined by ^{137}Cs, ^{26}Ra, and ^{210}Pb analyses of gravity cores collected at the same location and time as our sediment cores.[32] Comparison of XANES and EXAFS spectra from suboxic sediments at 1.5 cm depth and anoxic sediments at 34.5 cm (and deeper) suggest that most of the important trace metal chemistry occurs near the sediment–water interface and/or in the suboxic zone, where metal contaminates are strongly partitioned to sulfide or oxide phases. Once buried in the anoxic zone, the metal host phases are stable for long periods of time. X-ray absorption spectra

of shallow and deep sediments show that poorly crystalline cadmium and zinc sulfides form during biologically mediated sulfate reduction in the suboxic zone and remain stable in sediments with high HS^- concentrations for at least 50 to 60 years (to depths of 55 cm in deep cores). Thermodynamic calculations show porewater saturation or supersaturation with respect to both cadmium and zinc sulfide. Because of the high dissolved HS^- concentrations, metal sulfide aqueous complexes for several trace metals are stable and produce higher aqueous concentrations of contaminants with depth.

Similarly, we infer that association of lead with carbonate or phosphate phases, manganese with phosphate, and chromium with oxides or phyllosilicates occurs within the water column, the thin oxic sediment zone, or within the suboxic zone. X-ray absorption data show that the local atomic structure around these elements is independent of depth to 34.5 cm, suggesting association with thermodynamically stable or recalcitrant phases. Although the porewaters are saturated with respect to galena (PbS), there is no evidence for lead associated with sulfides in the XAS spectra. Lead may substitute for calcium in either calcite or apatite, both of which are thermodynamically stable based on porewater concentrations, or it may be present as a sorbed complex. Likewise, XANES spectra show that manganese is partially associated with a phosphate phase, which may indicate substitution in apatite or formation of $MnHPO_4$(s) as porewaters are close to $MnHPO_4$(s) saturation ($\log SI = -1$). As one might expect, chromium is present only as Cr(III) in these highly reduced sediments. XAS data suggest that dissolved anthropogenic chromium is removed from porewater by either precipitation of chromite or by sorption of chromium to phyllosilicates in the sediments. This is consistent with laboratory observations of Cr(III) sorption to micas and of the reduction of sorbed Cr(VI) by Fe(II) bearing micas.[33] The EXAFS data and the solution chemistry are also consistent with chromium association with oxides such as eskolaite, chromite or magnesiochromite, all of which are supersaturated. It is doubtful that chromium, lead, and manganese could be sorbed to iron (oxy)hydroxides below the oxic zone (about 1–2 cm) because XANES analysis indicates that available Fe(III) is not present below that depth.[29] Consequently, any chromium, lead, or manganese sorbed to iron (oxy)hydroxides in the water column or the oxic sediments would desorb and bond with oxides, phyllosilcates, carbonates, or phosphates below the zone of Fe(III) reduction.

Detrital phyllosilicates and oxides comprise a recalcitrant fraction of metals in these sediments. This conclusion is based on direct spectroscopic evidence, metal concentration profiles, and by comparison with metal concentrations in uncontaminated San Francisco Bay sediments.[21] The authigenic source of metals to San Francisco Bay sediments is the weathering of the ultramafic Franciscan formation, which can be seen in the iron and zinc oxide components. The iron oxide component is best described as recalcitrant phyllosilicate and oxide phases, probably as iron-bearing micas such as illite, muscovite, chlorite or biotite and oxides such as magnetite, chromite, or ilmenite[18] that do not dissolve in the strongly reducing sediments at neutral pH. It is likely that the zinc oxide fraction and part of the chromium and manganese fractions are associated with these unreactive phases. Comparison of the metal concentrations in the oxide components and in the surface sediments with metal concentrations in uncontaminated San Francisco Bay sediments further supports the detrital source for metals. Hornberger *et al.*[21] report background chromium concentrations of 125 to 150 $\mu g\ g^{-1}$, copper concentrations of 20 to 40 $\mu g\ g^{-1}$, lead concentrations of 5 $\mu g\ g^{-1}$, nickel concentrations of 75 to 100 $\mu g\ g^{-1}$, and zinc concentrations of 78 $\mu g\ g^{-1}$. These numbers compare well with zinc concentrations associated with the zinc oxide component estimated from EXAFS (50 to 130 $\mu g\ g^{-1}$), and surface sediment chromium (200 $\mu g\ g^{-1}$), copper (100 $\mu g\ g^{-1}$), and nickel (100 $\mu g\ g^{-1}$) concentrations. We cannot resolve the anthropogenic and detrital chromium components in the EXAFS, but the data are consistent with a partial detrital component. Seaplane Lagoon nickel and manganese concentrations are fairly constant and do not show the anthropogenic signature of increasing concentration with depth that is seen for the other trace metals. Therefore, it is possible that nickel and the non-phosphate manganese fraction are associated with detrital phyllosilicates. Almost all of the lead in the sediments is anthropogenic even in the surface sediments. Lead concentrations in the Seaplane Lagoon sediments range from 200 to 1400 $\mu g\ g^{-1}$, and are 40 to 280 times higher than in the uncontaminated San Francisco Bay sediments.

4.2 Metal geochemistry in oxidized sediments

Oxidation of reduced estuarine sediments may occur during dredging operations and during bioturbation or storm events at the interface between the surface sediments and the overlying water. In these environments, the oxidation of sulfides is an important source of dissolved cadmium, zinc, and possibly copper. However, their inherent hazard to biota is mitigated by their sorption to or co-precipitation with oxide substrates. Of these trace metals, cadmium is the most mobile because much less of it is precipitated as an oxide. In our study, about 63% of the CdS and 71% of the ZnS in the reduced sediments dissolved during the experiment, but only 50% of the reacted cadmium was taken up as an oxide, compared to 80% of the reacted zinc. These numbers are based on comparison of EXAFS analyses of the reduced and oxidized sediment, and on the net amount of metal dissolved during the experiment (Fig. 6 and 7). One explanation for the low uptake of cadmium compared to zinc is much higher cadmium aqueous complexation. In seawater, about 99% of the cadmium complexes with chloride and 1% is free cadmium ion. By contrast, only 32% of the zinc complexes with chloride and 58% is free zinc ion. This comparison suggests that free metal ions have much higher affinity for hydroxide surfaces than the metal complexes. Minimal cadmium sorption may also result from competition between zinc and cadmium. This phenomenon has been observed in laboratory and field studies. In laboratory experiments, cadmium sorption was suppressed by zinc and lead sorption to iron oxyhydroxide.[34,35] A field study of mine drainage sediments showed that iron (oxy)hydroxide effectively sorbs zinc.[16,36] We assume that copper is present as a sulfide at depth and sorbs to an oxide substrate when the sediment is oxidized, because the dissolution of copper with time is similar to the behavior of cadmium and zinc. All three elements exhibit a rapid increase in the dissolution rate followed by a decrease in the rate as they sorb to or co-precipitate with oxide substrates.

The most likely oxide substrate for cadmium and zinc uptake is precipitated iron (oxy)hydroxide from the dissolution of pyrite during the oxidation experiment. Pyrite is known to dissolve in seawater. Morse[37] report 20% oxidation of pyrite in seawater in one day. In our EXAFS spectra, we detected a 17% decrease in the pyrite fraction at the end of our oxidation experiment. It is likely that the decrease in the pyrite fraction was accompanied by the precipitation of an iron (oxy)hydroxide because almost no dissolved iron was measured in the oxidation experiments. Another possible oxide-substrate for cadmium and zinc uptake would be phyllosilicate phases present in the sediments. It is doubtful that cadmium and zinc co-precipitates with calcium carbonate because no calcite was detected in the X-ray diffraction patterns, nor do we have evidence from solution chemistry for calcite precipitation during the oxidation experiment. It is also doubtful that cadmium and zinc sorb to manganese (oxy)hydroxides because the concentrations of cadmium ($\sim$40 $\mu g\ g^{-1}$) and zinc ($\sim$210 $\mu g\ g^{-1}$) associated with the oxide component

approximate the total manganese ($\sim$210 μg g^{-1}) in non-phosphate component ($\sim$50–80%, which is probably associated with phyllosilicates). The non-phosphate and phosphate manganese components are stable in seawater. Although a small percentage of manganese dissolved during the first few hours of oxidation, no significant changes in the relative proportions of these phases were observed in the XANES spectra.

Oxidation of reduced contaminated sediments will not yield significant mobilization of chromium and lead because they are associated with oxides, phyllosilicates, carbonates or phosphates. Consequently, they are stable when exposed to oxygen-rich seawater and exhibit little dissolution. Additionally chromium retains its reduced oxidation state as Cr(III) when reacted with seawater. Although there is little difference in XAS spectra for the reduced and oxidized sediments, we cannot rule out the possibility that chromium and lead desorb and are taken up by the iron (oxy)hydroxides that forms as pyrite oxidizes.

5. Conclusions

The fate of metal contaminants in urban harbor and coastal sediments depends on the form of the stable solid phase that hosts the metal as sediments are buried and reduced, which cannot necessarily be predicted from the water chemistry. In the suboxic and anoxic sediments with elevated HS^- concentrations, anthropogenic cadmium and zinc form disordered sulfides, but anthropogenic lead and chromium are associated with stable oxides. In addition to the anthropogenic metals, some chromium, manganese, and zinc and all of the nickel appear to be associated with recalcitrant detrital minerals, quite possibly in iron-rich phyllosilicates and oxides. A fraction of manganese is also present as a phosphate. Cadmium and zinc pose the greatest hazard to biota during dredging, bioturbation, or storm events because these sulfides are unstable and will dissolve in oxygen-rich seawater. Dissolved cadmium and zinc will partially sorb to available phyllosilicates or oxides, or co-precipitate with iron (oxy)hydroxides that form as pyrite oxidizes. Uptake of cadmium and zinc by oxides significantly lowers their dissolved concentrations and reduces their overall hazard to biota. Dredging of deeper sediments poses a minimal hazard to biota for lead and chromium because they are associated with stable carbonate, phosphate, phyllosilicates or oxides. Additionally, chromium is present in its reduced from, Cr(III), in the sediments and showed no evidence for oxidation to Cr(VI) when reacted with seawater.

One significant observation from this study is that dominant reactions that remove dissolved metals from solution occur within the water column or the oxic and suboxic sediments, with minimal metal transformation within the anoxic sediments over time (and depth). As iron (oxy)hydroxides and sulfate are reduced at depths less than 5 cm, dissolved metals are taken-up by stable solids below the sediment–water interface. Once buried, the phases hosting the trace metals are stable for a minimum of 60 years (age of the sediments). Any cadmium and zinc associated with reactive iron (oxy)-hydroxides in the water column or in the oxic sediments will dissolve and re-precipitate as disordered sulfides with in suboxic sediments. In contrast, any lead bonded to stable phases such carbonate or phosphate in the oxygen-rich water column or in oxic sediments does not dissolve and re-precipitate as its thermodynamically stable sulfide phase (galena, PbS).

This work was motivated by the US Navy's concern that sediments contaminated prior to the Clean Water Act (1975) would contaminate the overlying water column as metals dissolve when reduced sediments react with oxygen-rich water during bioturbation, storm, dredging and other marina activities. The results of this study can be used to help design the impact of remediation strategies.

Acknowledgements

This work was supported by Alameda Naval Air Station BERC, University of California at Berkeley and was performed under the auspices of the Department of Energy by the Lawrence Livermore National Laboratory under Contract W-7405-Eng-48. Work at Arizona State University was done under subcontract B338664 from LLNL and supported by the National Science Foundation (EAR-9629276 to PAO). The XAS work was done at SSRL, which is operated by the DOE, Office of Basic Energy Sciences. We thank the SSRL Biotechnology Program, which is supported by the National Institutes of Health, National Center for Research Resources, Biomedical Technology Program, and the DOE, Office of Biological and Environmental Research. We thank Andrew Bono for assistance with sample and XAS data collection, Patrick Allen and Jerry Bucher for use of their Ge detector, Roger Martinelli for assistance with porewater analysis, and Ron Pletcher for assistance with processing of the sediment cores.

References

1 *The Incidence and Severity of Sediment Contamination in Surface Waters of the United States. Volume 1. National Sediment Quality Survey*, Environmental Protection Agency, 1997, #EPA 823-R-97-006.
2 *Draft EIR: For the reuse of Naval Air Station Alameda and the Fleet and Industrial Supply Center, Alameda Annex and Facility, Alameda, California*, City of Alameda, Alameda, 1999.
3 I. Rivera-Duarte and A. R. Flegal, Benthic lead fluxes in San Francisco Bay, California, USA, *Geochim. Cosmochim. Acta*, 1994, **58**, 3307–3313.
4 I. Rivera-Duarte and A. R. Flegal, Pore-water silver concentration gradients and benthic fluxes from contaminated sediments of San Francisco Bay, California, USA, *Mar. Chem.*, 1997, **56**, 15–26.
5 I. Rivera-Duarte and A. R. Flegal, Porewater gradients and diffusive benthic fluxes of Co, Ni, Cu, Zn, and Cd in San Francisco Bay, *Croat. Chim. Acta*, 1997, **70**, 389–417.
6 S. F. G. Westerlund, L. G. Anderson, P. O. J. Hall, A. Iverfeldt, M. M. R. van der Loeff and B. Sundby, Benthic fluxes of cadmium, copper, nickel, zinc, and lead in the coastal environment, *Geochim. Cosmochim. Acta*, 1986, **50**, 1289–1296.
7 B. Sunby, L. G. Anderson, P. O. J. Hall, A. Iverfeldt, M. M. R. van der Loeff and S. F. G. Westerlund, The effect of oxygen on release and uptake of cobalt, manganese, iron, and phosphate at the sediment–water interface, *Geochim. Cosmochim. Acta*, 1986, **50**, 1281–1288.
8 W. A. Kornicker and J. W. Morse, Interactions of divalent cations with the surface of pyrite, *Geochim. Cosmochim. Acta*, 1991, **55**, 2159–2171.
9 M. A. Huerta-Diaz and J. W. Morse, Pyritization of trace metals in anoxic marine sediments, *Geochim. Cosmochim. Acta*, 1992, **56**, 2681–2702.
10 T. Arakaki and J. W. Morse, Coprecipitation and adsorption of Mn(II) with mackinawite (FeS) under conditions similar to those found in anoxic sediments, *Geochim. Cosmochim. Acta*, 1993, **57**, 9–14.
11 C. A. Coles, S. R. Rao and R. N. Yong, Lead and cadmium interactions with mackinawite: Retention mechanisms and the role of pH, *Environ. Sci. Technol.*, 2000, **34**, 996–1000.
12 K. G. Knauss and T. J. Wolery, Dependence of albite dissolution kinetics on pH and time at 25 °C and 70 °C, *Geochim. Cosmochim. Acta*, 1986, **50**, 2481–2497.
13 J. W. Boyle and E. A. Wu, Low blank preconcentration technique for the determination lead, copper, and cadmium in small-volume seawater by isotope dilution ICPMS, *Anal. Chem.*, 1997, **69**, 2464–2470.
14 G. N. George and I. J. Pickering, *EXAFSPAK: A suite of computer programs for analysis of X-ray absorption spectra*, 1993, Stanford Synchrotron Radiation Laboratory, Palo Alto, CA.
15 J. J. Rehr, R. C. Albers and S. I. Zabinsky, High-order multiple scattering calculations of X-ray absorption fine structure, *Phys. Rev. Lett.*, 1992, **69**, 3397–3400.

16 P. A. O'Day, S. A. Carroll and G. A. Waychunas, Rock-water interactions controlling zinc, cadmium, and lead in surface waters and sediments: I. Molecular identification using X-ray absorption spectroscopy, *Environ. Sci. Technol.*, 1998, **32**, 943–955.
17 S. Carroll, B. Esser, S. Randal, P. O'Day, A. Bono and G. W. Luther, III, *Geochemical Characterization of Seaplane Lagoon Sediments, Alameda Naval Air Station, California*, LLNL-UCRL-ID−135193, Lawrence Livermore National Laboratory, Livermore, CA, 1999.
18 P. A. O'Day, N. Rivera and S. A. Carroll, *X-ray Absorption Spectroscopy Study of Iron Reference Compounds for the Analysis of Natural Sediments*. in preparation.
19 C. M. Bethke, *The Geochemist's Workbench: A users guide to Rxn, Act2, Tact, React, and Gtplot*, University of Illinois, Urbana-Champaign, IL, 2nd edn., 1994, p. 213.
20 J. W. Johnson, E. H. Oelkers and H. C. Helgeson, SUPCRT92: A softwater package for calculating the standard molal thermodynamic properties of minerals, gases, aqueous species, and reactions from 1 to 5000 bar and 0 to 1000 °C, *Comput. Geosci.*, 1992, **18**, 899–947.
21 M. I. Hornberger, S. N. Luoma, A. van Geen, C. Fuller and R. Anima, Historical trends of trace metals in the sediments of San Francisco Bay, California, *Mar. Chem.*, 1999, **64**, 39–55.
22 P. A. O'Day, S. A. Carroll, S. Randall, R. E. Martinelli, S. L. Anderson, J. Jelinski and J. Knezovich, Metal Speciation and Bioavailability in Contaminated Estuary Sediments, Alameda Naval Air Station, California, *Environ. Sci. Technol.*, 2000, **34**, 3665–3673.
23 J. R. Barger, G. E. Brown, Jr. and G. A. Parks, Surface complexation of Pb(II) at oxide–water interfaces: XAFS and bound-valence determination of mononuclear Pb(II) sorption products and surface functional groups on iron oxides, *Geochim. Cosmochim. Acta*, 1997, **61**, 2639–2652.
24 J. D. Ostergren, G. E. Brown Jr., G. A. Parks and T. N. Tingle, Quantitative speciation of lead in selected mine tailings from Leadville, CO, *Environ. Sci. Technol.*, 1999, **33**, 1627–1636.
25 J. E. Villinski, P. A. O'Day, T. L. Corley and M. H. Conklin, In situ spectrocopic and solution analyses of the reductive dissolution of MnO_2 by Fe(II), *Environ. Sci. Technol.*, 2001, **35**, 1157–1163.
26 J. E. Villinski, *Reductive dissolution of manganese(IV) oxides and precipitation of iron(III): Implications for redox processes in an alluvial aquifer affected by acid mine drainage*, 2001, The University of Arizona, Tucson, AZ.
27 P. A. O'Day, G. E. J. Brown and G. A. Parks, X-ray absorption spectroscopy of cobalt(II) multinuclear surface complexes and surface precipitates on kaolinite, *J. Colloid Interface Sci.*, 1994, **165**, 269–289.
28 C. Palache, H. Berman and C. Frondel, *Dana's System of Mineralogy*, 7th edn., 1944, pp. 210–215.
29 P. A. O'Day, S. A. Carroll, S. Randall, A. Bono and G. W. Luther (III), *Iron Speciation in reduced estuarine sediments from in situ spectroscopy and microelectrode measurements*, in preparation.
30 L. Spadini, A. Manceau, P. W. Schindler and L. Charlet, Structure and stability of Cd^{2+} surface complexes on ferric oxides 1. Results from EXAFS spectroscopy, *J. Colloid Interface Sci.*, 1994, **168**, 73–86.
31 S. R. Randall, D. M. Sherman, K. V. Ragnarsdottir and C. R. Collins, The mechanism of cadmium surface complexation on iron oxyhydroxide minerals, *Geochim. Cosmochim. Acta*, 1999, **63**, 2971–2987.
32 A. H. Love, B. K. Esser and J. R. Hunt, Reconstructing contaminant deposition in a San Francisco Bay Marina, *J. Environ. Eng.*, 2002, submitted.
33 E. S. Ilton and D. R. Veblen, Chromium sorption by phlogopite and biotite in acidic solutions at 25 °C: Insights from X-ray photoelectron spectroscopy and electron microscopy, *Geochim. Cosmochim. Acta*, 1994, **58**, 2777–2788.
34 M. M. Benjamin and J. O. Leckie, *Adsorption of metals at oxide interfaces: Effects of the concentrations of adsorbate and competing metals*, in *Contaminants and Sediments*, ed. R. A. Baker, 1980, American Chemical Society, New York.
35 M. M. Benjamin and J. O. Leckie, Multiple-site adsorption of Cd, Cu, Zn, and Pb on amorphous iron oxyhydroxide, *J. Colloid Interface Sci.*, 1981, **79**, 209–221.
36 S. A. Carroll, P. A. O'Day and M. Piechowski, Rock-water interactions controlling zinc, cadmium, and lead concentrations in surface waters and sediments: II. Geochemical interpretation, *Environ. Sci. Technol.*, 1998, **32**, 956–965.
37 J. W. Morse, Oxidation kinetics of sedimentary pyrite in seawater, *Geochim. Cosmochim. Acta*, 1991, **55**, 3665–3667.
38 V. A. Pokrovskii and H. C. Helgeson, Thermodynamic properties of aqueous species and the solubilities of minerals at high pressures and temperatures: The system Al_2O_3–H_2O–NaCl, *Am. J. Sci.*, 1995, **295**, 1255–1342.
39 H. C. Helgeson, J. M. Delany, H. W. Nesbitt and D. K. Bird, Summary and critique of the thermodynamic properties of rock-forming minerals, *Am. J. Sci.*, 1978, **278-A**, 1–229.
40 R. A. Robie, B. S. Hemingway and J. S. Fisher, Thermodynamic properties of minerals and related substances at 298.15 K and 1 bar (105 Pascals) pressure and at higher temperatures, *US Geol. Survey Bull.*, 1979, **1452**, 1–456.
41 C. F. J. Baes and R. E. Mesmer, *The Hydrolysis of Cations*, Wiley-Interscience, New York, 1976.
42 D. A. Sverjensky, E. L. Shock and H. C. Helgeson, Prediction of the thermodynamic properties of aqueous metal complexes to 1000 degrees C and 5 kb, *Geochim. Cosmochim. Acta*, 1997, **61**, 1359–1412.
43 S. L. S. Stipp, G. A. Parks, D. K. Nordstrom and J. O. Leckie, Solubility-product constant and thermodynamic properties for synthetic otavite, $CdCO_3$(s), and aqueous association constants for the Cd(II)–CO_2–H_2O system, *Geochim. Cosmochim. Acta*, 1993, **57**, 2699–2714.
44 D. D. Wagman, W. H. Evans, V. B. Parker, R. H. Schumm, I. Halow, S. M. Bailey, K. L. Churney and R. L. Nuttall, The NBS tables of chemical themodynamic properties, *J. Phys. Chem. Ref. Data*, 1982, **11**(suppl. 2), .
45 R. Al-Farawati and C. M. G. van den Berg, Metal-sulfide complexation in seawater, *Mar. Chem.*, 1999, **63**, 331–352.
46 J. D. Cox, D. D. Wagman and V. A. Medvedev, *CODATA Key Values for Thermodynamics*, Hemisphere, New York, 1989.
47 I. Dellien, F. M. Hall and L. G. Helper, Chromium, molybdenum, tungsten: Thermodynamic properties, chemical equilibria, and standard potentials, *Chem. Rev.*, 1976, **76**, 283–310.
48 G. W. Luther (III), S. M. Theberge, D. T. Richard and A. Oldroyd, Determination of metal (bi)sulfide stability constants of Mn^{2+}, Fe^{2+}, Co^{2+}, Ni^{2+}, and Zn^{2+} by voltammetric methods, *Environ. Sci. Technol.*, 1996, **30**, 671–679.
49 H. C. Helgeson, Thermodynamics of hydrothermal systems at elevated temperatures and pressures, *Am. J. Sci.*, 1969, **267**, 729–804.
50 T. J. Wolery, *Some aspects of hydrothermal processes at mid-ocean ridges — A theoretical study. I. Basalt-sea water reaction and chemical cycling between the ocean crust and the oceans. II. Calculation of chemical equilibrium between aqueous solutions and minerals*, 1978, Northwestern University, Evanston, IL.
51 D. J. Vaughan and J. R. Craig, *Mineral Chemistry of Metal Sulfides*, 1978, Cambridge University Press, Cambridge, UK.
52 R. M. Smith and A. E. Martell, *Critical Stability Constants*, New York, Plenum Press, 2nd edn., 1989, **vol. 4**, p. 256.
53 H. Bilinski and P. Schindler, Solubility and equilibrium constants of lead in carbonate solutions, *Geochim. Cosmochim. Acta*, 1982, **46**, 921–928.
54 W. L. Bourcier and H. L. Barnes, Ore Solution Chemistry - VII. Stabilities of chloride and bisulfide complexes of zinc to 350 °C, *Econ. Geol.*, 1987, **82**, 1839–1863.
55 J. M. Zachara, J. A. Kittrick, L. S. Dake and J. B. Harsh, Solubility and surface spectroscopy of zinc precipitates on calcite, *Geochim. Cosmochim. Acta*, 1989, **53**, 9–20.
56 G. W. Luther (III), S. M. Theberge and D. T. Rickard, Evidence for aqueous clusters as intermediates during zinc sulfide formation, *Geochim. Cosmochim. Acta*, 1999, **63**, 3159–3169.
57 P. Schindler, M. Reinert and H. Gamsjager, Loslichkeitskostanten und free buildungsenthalpien von $ZnCO_3$ und $Zn_5(OH)_6(CO_3)_2$ bei 25 °C, *Helv. Chim. Acta*, 1969, **52**, 2327–2332.
58 F. G. Smith, Lattice dimensions of cadmium sulfide, *Am. Mineral.*, 1955, **40**, 696–697.
59 F. Jellinek, The structure of chromium sulfides, *Acta Crystallogr.*, 1957, **10**, 620–628.
60 G. Brunton, Refinement of the structure of $K_2Cr_2O_7$, *Mater. Res. Bull.*, 1973, **8**, 271–274.
61 N. Elliot, Interatomic distances in FeS_2, CoS_2, and NiS_2, *J. Chem. Phys.*, 1960, **33**, 903–905.
62 G. George, personal communication.